Solid Earth
Discussions

Open Access

EGU

1

2   Sedimentary mechanisms of a modern banded iron formation on

3   Milos Island, Greece

4

5   [1,2]Ernest Chi Fru*, [3]Stephanos Kilias, [4]Magnus Ivarsson, [1]Jayne E. Rattray, [3]Katerina

6   Gkika, [2]Iain McDonald, [5]Qian He, [1]Curt Broman

7

8   [1]Department of Geological Sciences, 10691, Stockholm University, Sweden.

9   [2]School of Earth and Ocean Sciences, Cardiff University, Park Place, CF10 3AT,

10   Cardiff, UK.

11   [3]Department of Economic Geology and Geochemistry, Faculty of Geology and

12   Geoenvironment, National and Kapodistrian University of Athens, Panepistimiopolis,

13   Zographou, 15784, Athens, Greece.

14   [4]Department of Palaeobiology, Swedish Museum of Natural History, Box 50007,

15   Stockholm, Sweden.

16   [5]School of Chemistry, Cardiff University, Park Place, CF10 3AT, Cardiff, UK.

17

18   *Corresponding author

19   Tel: +44(0)29 208 70058

20   Email: ChiFruE@cardiff.ac.uk

21

22

23

24   Short title: A modern banded iron formation

Abstract. An Early Quaternary shallow submarine hydrothermal iron formation (IF)
in the Cape Vani sedimentary basin (CVSB) on Milos Island, Greece, displays banded
rhythmicity similar to Precambrian banded iron formation (BIF). Sedimentary,
stratigraphic reconstruction, biogeochemical analysis and micro-nanoscale
mineralogical characterization confirms the Milos rocks as modern Precambrian BIF
analogues. Spatial coverage of the BIF-type rocks in relation to the economic grade
Mn ore that brought prominence to the CVSB implicates tectonic activity and
changing redox in the deposition of the BIF-type rocks. Field-wide stratigraphic and
biogeochemical reconstruction demonstrates two temporal and spatially isolated iron
deposits in the CVSB with distinct sedimentological character. Petrographic screening
suggest the previously described photoferrotrophic-like microfossil-rich IF (MFIF),
accumulated on basement andesite in a ~150 m wide basin, in the SW margin of the
basin. A strongly banded non-fossiliferous IF (NFIF) caps the Mn-rich sandstones at
the transition to the renowned Mn-rich formation. Geochemical evidence relates the
origin of the NFIF to periodic submarine volcanism and water column oxidation of
released Fe(II) in conditions apparently predominated by anoxia, similar to the MFIF.
This is manifested in the lack of shale-normalized Ce anomalies. Raman spectroscopy
pairs hematite-rich grains in the NFIF with relics of a carbonaceous material carrying
an average $\delta^{13}C_{org}$ signature of ~-25‰. However, a similar $\delta^{13}C_{org}$ signature in the
MFIF is not directly coupled to hematite by mineralogy. The NFIF, which post dates
large-scale Mn deposition in the CVSB, is composed primarily of amorphous Si
(opal-$SiO_2 \cdot nH_2O$) while crystalline quartz (SiO_2) predominates the MFIF. An
intricate interaction between tectonic processes, changing redox, biological activity
and abiotic Si precipitation, formed the unmetamorphosed BIF-type deposits.

Keywords: Banded iron formation; BIF analogue; Hydrothermal activity; Iron
cycling; Silica cycling.

61   **1 Introduction**

62   Recently, an Early Quaternary iron formation (IF), ~2.0 million years old, displaying

63   banded rhythmicity typical of Precambrian banded iron formations (BIF) (James,

64   1954; Gross, 1980; Simonson, 1985, 2003; Bekker et al., 2010), was serendipitously

65   discovered in the Cape Vani sedimentary basin (CVSB) on Milos Island, Greece (Chi

66   Fru et al., 2013, 2015). Before this discovery, Cape Vani was long known to host Mn

67   oxide ores of economic potential (Hein et al., 2000; Liakopoulos et al., 2001; Glasby

68   et al., 2005; Kilias et al., 2007). Milos is an emergent volcano on the Hellenic

69   Volcanic Arc (HVA) where arc-volcanism and seafloor hydrothermal activity occur

70   in thinned pre-Alpine to Quaternary continental crust (Kilias et al., 2013) (Fig. 1). The

71   first reported IF from Cape Vani is unmetamorphosed and contains diverse

72   microfossils encrusted by hematite, with ferrihydrite proposed as a primary precursor

73   mineral (Chi Fru et al., 2013, 2015). Field stratigraphy, Rare Earth Elements (REEs),

74   stable isotopes, petrographic and microfossil studies point to microbial Fe deposition

75   in a semi-enclosed, shallow submarine basin under conditions analogous to those that

76   formed the Precambrian Algoma-type BIFs near volcanic centers (Chi Fru et al.,

77   2015). These earlier reports assumed a one-time basin-wide depositional event and a

78   common origin for all Fe-rich sedimentary rocks in the CVSB.

79   However, it remains unclear what sedimentary processes caused the distinct

80   deposition of the BIF-type rocks in a basin where Mn precipitation was apparently

81   widespread at various intervals. Moreover, it is not known how the Mn ores relate

82   temporally and spatially to Fe deposition in the ~1 km long CVSB. This knowledge

83   may provide clues to processes that triggered large-scale deposition of similar

84   Proterozoic Fe-Mn-rich deposits (Roy, 2006; Tsikos et al., 2010). Here, new

85   sedimentological, petrological and biogeochemical evidence describes cycles of

86   periodic precipitation of shallow submarine Si and Fe-rich sedimentary rocks and the

87   plausible mechanisms that enabled their temporal and spatial separation from the Mn

88   deposits in the CVSB. The data reveal a much more complex depositional system not

89   only controlled by microbial Fe(II) oxidation as previously proposed (Chi Fru et al.,

90   2013, 2015), but illuminates episodic volcanism coupled to changing redox conditions

91   as a central mechanism in the formation of the banded iron rocks.

92

93   **1.1 Geological setting**

94   The geology and, iron and manganese mineralization of the CVSB have been

95   described in detail (Plimer, 2000; Hein et al., 2000; Liakopoulos et al., 2001;

96   Skarpelis and Koutles, 2004; Glasby et al., 2005; Stewart and McPhie, 2006; Kilias,

97   2011; Alfieris et al., 2013: Chi Fru et al., 2013, 2015; Papavassiliou et al., 2017).

98   Briefly, the Milos IF is part of the CVSB, a recently emergent sedimentary rift basin

99   located NW of Milos Island, along the HVA in the Aegean Sea, Greece (Fig. 1). It

100   hosts a fossil analogue of active shallow-submarine hydrothermal activity on the coast

101   of Milos Island (Dando et al., 1995). The CVSB developed within a 2.7 to 1.8 Ma

102   shallow-submarine rhyolitic-dacitic volcanic center, filled up mainly by a ~35-50 m

103   thick stratigraphic succession of volcaniclastic/epiclastic sandstones and sandy tuffs

104   spanning Upper Pliocene to Lower Pleistocene, 35-40% of which is hydrothermally

105   mineralized by Mn oxides and barite (Hein et al., 2000; Liakopoulos et al., 2001;

106   Skarpelis and Koutles, 2004; Papavassiliou et al., 2017). Sedimentologic and

107   ichnologic data, including sedimentary structures, lamellibranch, echinoid and

108   brachiopod fossils, the gastropod mollusk fossil, Haustator biplicatus (Bronn, 1831),

109   and microbially induced sedimentary structures (e.g., Kilias, 2011), suggest that most

110   of the CVSB sandstones/sandy tuffs hosting the Mn-rich deposit, are foreshore to

111   shoreface shallow submarine deposits, formed at a maximum depth of 200 mbsl. Over

112   the last 0.8 Myr, fluctuating water depths due to sea-level changes of up to 120 m and

113   volcanic edifice building, has resulted in tectonic uplift of ~250 m (Papanikolaou et

114   al., 1990). The CVSB fill, currently 35 m above sea level, is tectonically northbound

115   by intrusive rhyolite, framed by elevated andesitic-dacitic centres, with the Cape Vani

116   and the Katsimoutis dacitic lava domes being the most prominent (Fig. 1).

117

118   **2 Methodology**

119   **2.1 Sample preparation**

120   Sedimentary structures, grain-size trends, lateral facies variations, vertical stacking

121   trends, and key stratigraphic surfaces form the basis for facies analysis. Prior to

122   mineralogical and geochemical analysis, exposed rock surface layers were sawn and

123   removed.   GeoTech Labs (Vancouver, Canada) produced doubly polished thin

124   sections for mineralogical and textural analysis, while geochemical analysis was

125   performed on pulverized powders and acid-digests (Chi Fru et al., 2013, 2015).

126

127   **2.2 Mineralogical analysis**

128   **2.2.1 X-Ray Diffraction analysis**

129   A PANalytical Xpert-pro diffractometer at room temperature, 45 kV, 40 mA and

130   1.5406 Å wavelength and Cu-Kα radiation and Ni-filter, was used for Powder X-Ray

131   Diffraction (PXRD) analysis. Samples were analyzed between 5-80° in step sizes of

132   0.017° with continuous mode scanning step time of 50.1650 s while rotating. Raman

133   spectroscopy was performed with a confocal laser Raman spectrometer (Horiba

134   instrument LabRAM HR 800), equipped with a multichannel air-cooled (-70°C) 1024

135   x 256 pixel charge-coupled device (CCD) array detector as previously described (Chi

Solid Earth
Discussions

136   Fru et al. 2013, 2015). Spectral resolution was ~0.3 cm^{-1}/pixel.   Accuracy was

137   determined by a repeated silicon wafer calibration standard at a characteristic Raman

138   line of 520.7 cm^{-1}.

139

140   **2.2.2 Transmission electron microscopy**

141   Specimens for Transmission electron microscopy (TEM) were prepared from the

142   crushed rock specimen powder. This was followed by dry-dispersal onto a 300 mesh

143   holey carbon TEM Cu grid. Microscopy was conducted using a JEOL 2100 TEM

144   with a LaB$_6$ source in the School of Chemistry, Cardiff University, operated at

145   200kV. The X-EDS analysis was performed with an Oxford Instrument SDD detector

146   X-Max^N 80 T.

147

148   **2.2.3 Scanning electron microscopy**

149   Scanning Electron Microscopy-Energy Dispersive Spectroscopy (SEM-EDS) analysis

150   was done on a FEI QUANTA FEG 650 ESEM. Images were captured at 5 kV and

151   EDS data collected at 20 kV, using an Oxford T-Max 80 detector (Oxford

152   Instruments, UK). The analyses were performed in low vacuum to minimize surface

153   charging of uncoated samples. EDS elemental maps were collected for 30 min or until

154   the signal had stabilized, indicated by a clear distribution trend. The data were further

155   processed with the Oxford Aztec software.

156

157   **2.3 Geochemical analysis**

158   **2.3.1 Laser ablation ICP-MS and trace element analysis**

159   Laser Ablation-Inductively Coupled Plasma-Mass Spectrometry (LA-ICP-MS) was

160   performed at Cardiff University on polished thin sections. The LA-ICP-MS system

Solid Earth

Discussions

Open Access

161   comprised a New Wave Research UP213 laser system coupled to a Thermo X Series

162   2 ICP-MS. The laser was operated using a frequency of 10 Hz at pulse energy of

163   ~5mJ for an 80µm diameter beam using lines drawn perpendicular to the layering and

164   at a movement speed of 26 microns sec^{-1}. Samples were analyzed in time resolved

165   analysis (TRA) mode using acquisition times of between 110 and 250 seconds;

166   comprising a 20 second gas blank, 80-220 second ablation and 10 second washout.

167   Dwell times varied from 2 msec for major elements to 35 msec for low abundance

168   trace elements. Blank subtraction was carried out using the Thermo Plasmalab

169   software before time resolved data were exported to Excel.

170   Separated and independently pulverized banded layers were digested by lithium

171   borate fusion followed by major, trace and rare earth element (REE) analyses using

172   ICP-ES/MS and XRF at AcmeLabs® (http://acmelab.com). Geochemical data were

173   compared with previously published results for the more widely investigated Mn

174   deposits (Hein et al., 2000; Liakopoulos et al., 2001; Glasby et al., 2005).

175

176   **2.3.2 Isotope analysis**

177   C, N and S isotopic composition for the pulverized samples was determined as

178   previously described (Chi Fru et al., 2013, 2015), following combustion in a Carlo

179   Erba NC2500 analyzer and analyzed in a Finnigan MAT Delta V mass spectrometer,

180   via a split interface to reduce gas volume. Reproducibility was calculated to be better

181   than 0.15‰ for δ^{13}C and δ^{15}N and 0.2‰ for δ^{34}S. Total C and N concentrations were

182   determined simultaneously when measuring the isotope ratios. The relative error was

183   <1% for both measurements. For carbon isotopic composition of organic carbon,

184   samples were pre-treated with concentrated HNO_3 prior to analysis.

185

2.4 Organic geochemistry analysis

186

187   Lipid biomarker and compound specific $\delta^{13}C$ analyses were executed on powdered

188   samples of sectioned bands from which exposed surface layers had been removed.

189   Modern sediments from Spathi Bay, 36°40'N, 24°31'E, southeast of Milos Island,

190   collected by push coring at 12.5 m below the seafloor were freeze-dried prior to

191   extraction to aid the identification of potential syngenetic biomarkers in the

192   Quaternary rocks. Between 4-6 g of ground samples were ultrasonically extracted

193   using 3×Methanol, 3×(1:1) Methanol:Dichloromethane (DCM), and 3×DCM and

194   extracts were combined and dried under N_2. Samples were subsequently re-dissolved

195   in DCM then methylated following the method of Ichihara and Fukubayashi (2010).

196   The resulting residue was silylated using, 20 µl pyridine and 20 µl BSTFA and heated

197   at 60°C for 15 min. Total lipid extracts were analyzed using a Shimadzu QP 2010

198   Ultra gas chromatography mass spectrometer (GC/MS). Separation was performed on

199   a Zebron ZB-5HT column (30 m x 0.25 mm x 0.10 µm) with a helium carrier gas

200   flow at 1.5 ml min^{-1}. Samples were injected splitless, onto the column at 40°C with

201   the subsequent oven temperature program ramped to 180°C at a rate of 15°C min^{-1},

202   followed by ramping to 325°C at a rate of 4°C min^{-1} and a final hold for 15 min. The

203   MS was set to scan from 50 to 800 m/z with an event time of 0.70 sec and a scan

204   speed of 1111 u/sec. All peaks were background subtracted and identification

205   confirmed using the NIST GC/MS library and literature spectra. Contamination was

206   not introduced into the samples, as blank samples worked up concurrently with the

207   rock fractions had results comparable to the ethyl acetate instrument blank.

208

209   **2.5 Chemical weathering analysis**

210 Chemical index of alternation (CIA) was used to determine whether variations in

211 chemical weathering intensities would in addition to hydrothermal activity deliver

212 materials into the depositional basin from the continent, according to the

213 formula: $CIA = Al_2O_3/(Al_2O_3 + CaO + Na_2O + K_2O) \times 100$.   Extensively

214 applied, the CIA index reveals subtle changes in weathering fluxes (Nesbit and

215 Young, 1982; Maynard, 1993; Bahlburg & Dobrzinski, 2011), where increasing CIA

216 values generally indicate amplified chemical dissolution of rocks and selective release

217 of dissolvable CaO, Na_2O and K_2O into solution (Nesbit & Young, 1982; Maynard,

218 1993; Bahlburg & Dobrzinski, 2011). The broken rock particles enriched in the

219 poorly soluble Al_2O_3 fraction, settle to the seafloor as weathered sediments carrying a

220 chemical composition different from the source. In the absence of chemical

221 dissolution, no net chemical change is expected in the composition of sediments

222 compared to source and thus a low CIA index. CIA indices for detritus of 0-55, 55-75

223 and >75, are considered unweathered, unweathered to slightly weathered and

224 weathered to highly weathered, respectively (Nesbit & Young, 1982; Maynard, 1993;

225 Bahlburg & Dobrzinski, 2011). The redox conditions under which sediments formed

226 were obtained from REE composition normalized to the North American Shale

227 Standard (NASC) (Groment et al., 1984).

228

229 **3 Results**

230 **3.1 Lithostratigraphy**

231 Field-wide sedimentological and lithostratigraphical mapping of the CVSB in the

232 summer and fall of 2014, enabled the assessment of the lateral and vertical coverage

233 of the Milos iron oxide-rich facies relative to the Mn-rich sandstones that dominate

234 the Early Quaternary sedimentary basin (Fig. 2). Six stratigraphic sections,

235   representing marine siliciclastic lithofacies sequences, were investigated along a ~1

236   km SW-NE trending portion of the CVSB infill (Supplementary Figs 1-7). Sequence

237   stratigraphy was conducted on outcrops and vertical shafts and tunnels left behind by

238   extinct Mn mining activity. Two of those sections; Section A located at

239   36°44'17.85''N, 24°21'17.72''E and Section B located at 36°44'35.11''N,

240   24°21'11.25''E, contain stratigraphic units composed of layered, bedded, or

241   laminated rocks that contain ≥15 % Fe, in which the Fe minerals are commonly

242   interlayered with quartz or chert, in agreement with the definition of Precambrian

243   BIFs (James, 1954; Gross, 1980; Bekker et al., 2010). These IFs are descriptively

244   referred to here as microfossiliferous iron formation (MFIF) according to Chi Fru et

245   al. (2013, 2015), and non-microfossiliferous iron formation (NFIF) (this study),

246   respectively (Fig. 2). The MFIF and the NFIF occupy at most ~20% of the entire

247   CVSB infill.   The stratigraphy and sedimentary lithofacies are illustrated below,

248   using lithofacies codes modified after Bouma (1962), Miall (1978, 1985), Lowe

249   (1982), Mutti (1992) and Shanmugam (2016).

250   Further field stratigraphic survey revealed considerable lithologic variability

251   within three fault-bounded volcanosedimentary sub-basins in the CVSB (Fig. 2),

252   which for the sake of simplicity are referred to as Basin 1—host of the MFIF; Basin

253   2—host of economic grade Mn ore; and Basin 3—host of the NFIF (Fig. 2). Each

254   section is framed by distinct marginal normal faults that strike in the NW-SE and NE-

255   SW to NNE-SSW directions, distinguishable by distinct lateral sedimentary facies

256   exhibiting unique vertical sequence stratigraphy (Fig. 2; Supplementary Figs 1-7).

257   Faulting in the CVSB is related to major geographical activation of extensional

258   structures at intervals that shaped Milos into a complex mosaic of neotectonic units

259   (Papanikolaou et al., 1990).

Solid Earth
Discussions

260

3.1.1 Section A (36°44'17.85''N, 24°21'17.72''E)

261

262 Informally known as "Little Vani", Section A is the type section containing the MFIF

263 at the base. It crops out in the W-SW edge of the CVSB (Figs 1 & 2) as a ~6-7 m high

264 cliff resting stratigraphically on submarine dacitic and andesitic lavas and domes.

265 This section extends laterally in the N-NE direction for an estimated 300–500 m.

266 The MFIF is correlatively interpreted to be in direct stratigraphic contact with

267 Late Pliocene-Early Pleistocene (2.5–1.5 Ma) basement submarine dacitic-andesitic

268 rocks. Lithologically, the MFIF comprises laminated and massive fine-grained red

269 and white weathered ferruginous jaspelitic red chert layers (Chi Fru et al., 2013,

270 2015). The chert layers contain morphologically distinct Fe minerals dispersed in a

271 fine-grained siliceous matrix (Fig. 3), marked by the notable absence of pyrite and an

272 extremely low S content (Chi Fru et al., 2013, 2015). Layers are tabular and typically

273 laterally continuous at scales of several meters, whereas wave and current structures

274 (e.g., cross-lamination), are generally absent from the MFIF. The hematite-rich MFIF

275 laminae (Table 1) are built by massive encrustation of anoxygenic photoferrotrophic-

276 like microbial biofilms by precipitated Fe (Chi Fru et al., 2013). The base of the MFIF

277 outcrop, is visibly mineralized by black diffused bands/veins composed of Mn oxides

278 (Fig. 4 & Table 1).

279 A markedly reddish 2-3 m-thick section immediately overlies the MFIF,

280 comprising a distinct package of Fe-rich beds that transition up the section from fine

281 to reddish medium and coarse-grained to pebble–cobble conglomerate volcaniclastic

282 sandstone beds (Figs 4A & 5). The lower 1-2 m consist of fine-grained sandstone

283 beds that are well to moderately sorted, containing a 20-40 cm thick portion

284 dominated by plane parallel-laminated sandstone/sandy tuff, massive to plane

11

285 parallel-laminated sandstone/sandy tuff, and massive sandstone/sandy tuff lithofacies

286 (Fig. 5; Supplementary Fig. 1). The fabric of these Fe-rich sandstone facies consists

287 of sub-angular to sub-rounded and 100–600 μm fine to medium-grained volcaniclastic

288 K-feldspar grains, making up to 75% of the total rock, with variable amounts of

289 quartz and clay mineral grains.

290 The latter are overlain by a ~1-1.5 m sequence of poorly-sorted tabular clast-

291 supported pebble-to-cobble conglomerate beds with an erosional base, grading

292 upward into coarse to medium-grained Sh beds, arranged in alternating conglomerate

293 cycles (Fig. 5), averaging 20-40 cm in thickness. The cobble/pebble conglomerate

294 clasts include intraformational volcanic rocks (dacite, andesite), allochthonous

295 volcaniclastic sandstone, and volcaniclastic microclasts (e.g. K-feldspar), cemented

296 by hematite (Fig. 5; Chi Fru et al., 2013; Kilias et al., 2013). Towards the

297 westernmost edge of the "Little Vani" section, there is a facies change from the

298 graded Gcm/Sh rhythms to a predominantly Fe-rich conglomerate Gcm bed (Fig. 4A),

299 termed the conglomerate-hosted IF (CIF) in Chi Fru et al. (2015), with a maximum

300 thickness of ~0.5 m and a cobble size range of ~10 cm. The Fe-rich conglomerate bed

301 transitions upward into medium-grained pebbly reddish ferruginous Sm with thin

302 volcanic rock and sandstone pebble lenses. This in turn grades upwards into a very-

303 fine-grained greenish glauconite-bearing plane parallel-laminated sandstone to

304 siltstone bed; characterized by soft-sediment deformation structures, such as flame

305 structures, convolute bedding and lamination structures, loop bedding, load casts, and

306 pseudonodules (Supplementary Figs 1-2).

307 The "Little Vani" section is eventually capped along an erosional surface by

308 an overlying 1-2 m thick section dominated by medium to fine-grained and

309 moderately to poorly-sorted reddish Fe-rich tabular sandstone beds, 10–40 cm thick,

310 topped by patchy sub-cm to cm-thick Mn-rich sandstones (Fig. 5; Supplementary Figs

311 1-2). Dominant lithofacies of the Fe-rich sandstone cap include planar and hummocky

312 cross-bedding, exhibiting bioturbation in places. The Fe-rich lithofacies cap is

313 laterally discontinuous, thinning out basinwards towards the N-NE, and can be

314 observed smoothly grading into a 1-2 m thick section composed of cm to sub-cm-

315 thick Mn–rich volcaniclastic sandstone lithofacies, described below in Section B. No

316 Fe-rich hydrothermal feeder veins are obvious in the MFIF, however feeder veins and

317 Mn horizons can be observed to truncate laminations in the MFIF, and up through the

318 whole "Little Vani" section (e.g., Figs 4C & 5).

319

320 **3.1.2 Interpretation of Section A**

321 The MFIF rests directly on the submarine dacites-andesites that were deposited in

322 relatively shallow but dominantly below a wave base submarine setting (Stewart and

323 McPhie, 2006). The fine-grained, finely laminated nature of the MFIF, and, the lack

324 of evidence of current or wave structures (e.g., symmetric ripples or hummocky

325 cross-stratification), coupled to the absence of volcanogenic detrital particles and

326 intraclast breccia structures, indicate a low energy sedimentation environment at ca. ≥

327 100-200 m depth, marked by negligible volcanic interference (e.g., Tice and Lowe,

328 2006; Trower and Lowe, 2016; Konhauser et al., 2017). This interpretation is

329 supported by the observed enrichment of Fe in the MFIF; a characteristic of relatively

330 deeper water lithofacies (Trower and Lowe, 2016; Konhauser et al., 2017). This view

331 is compartible with the proposition that hematite enrichment in the MFIF was under

332 the control of photoferrotrophic biofilms (Chi Fru et al., 2013) known to thrive at

333 lower light intensities (Kappler et al., 2005; Li et al., 2013; Konhauser et al., 2017).

334 The quiet environmental conditions would have ensured the formation of such stable

335   photoferrotrophic biofilms over extended periods of time that would have facilitated

336   the oxidation of hydrothermally released Fe(II) and the depositon of Fe(III) minerals.

337   The overlying lithofacies sequence record a switch to faster accumulation of

338   volcaniclastic turbidites on the quiet MFIF deposit, with the fine, medium to coarse-

339   grained sandstone lithofacies typifying deposition during low and high density

340   turbiditic flows in the middle to inner parts of a turbidite fan-like environment (Lowe,

341   1982; Mutti 1992; Talling et al., 2012; Orme and Laskowski, 2016; Shanmugam,

342   2016; Wang et al., 2017). Massive conglomerates containing both allochthonous

343   sandstone clasts and intraformational andesite-dacite are interpreted as channelized

344   submarine debris flows or slump deposits sourced from adjacent topographic highs

345   (Lowe, 1982; Stewart and McPhie, 2006; Orme and Laskowski, 2016). Also,

346   deposition from a waning low density turbidity current is indicated by the upward

347   fining bed of pebbly Fe-rich sandstone, greenish glauconite bearing sandstone and

348   laminated siltstone. Up section, the abundance of parallel and cross stratified Fe-rich

349   and Mn-rich sandstone facies along an erosional surface, reflect a change in

350   deposition to a high energy, shallow submarine shoreface/foreshore setting, above a

351   wave base.

352   In summary, stratigraphic observations in the "Little Vani" section indicate that

353   the MFIF constitutes the older IF deposited on the CVSB basement lavas. Following

354   MFIF deposition, there have been a series of upward lithologic changes which reflect

355   gradual shoaling, accompanied by tectonic instability, topographic growth, submarine

356   erosion, and massive sediment supply by density/gravity flows of volcanogenic

357   debris. It is proposed that these changes were controlled by a combination of

358   submarine volcano-constructional processes, synvolcanic rifting and volcano-tectonic

359   uplift, resulting in cyclic changes in depositional water depth (Stewart and McPhie,

360 2006; Papanikolaou et al., 1990; Steele et al., 2000; Trower and Lowe, 2016; Wang et

361 al., 2017).

362

363 **3.2 Section B (36°44'35.11''N, 24°21'11.25''E)**

364 This ~8-10 m-thick fault-bounded stratigraphic section, here referred to as "Magnus

365 Hill", is the type section that contains the NFIF (Figs 2 & 7; Supplementary Figs 3-4).

366 Two lithostratigraphic units—a lower unit A and an upper unit B—are identified in

367 this study. Unit A is made up of a lower sandstone facies that is ~4-5 m thick,

368 dominated by a Mn-oxide cement exhibiting a grayish to black, coarse to very coarse-

369 grained volcaniclastic sandstone beds, overlain by reddish brown Fe-rich massive

370 sandstone beds (Fig. 8 & Supplementary Figs 3-4). Unit B, ~5 m thick,

371 unconformambly overlies unit A and comprises two distinct packages of beds that

372 transition up section from brownish gravel-to-pebble conglomerate beds (0.5-1.0 m

373 thick), in contact with the very fine-grained NFIF deposit (Supplementary Fig. 8 & 9).

374 The NFIF is capped by patchy cm-thick crustiform Mn oxides. Bifurcating feeder

375 veins composed of barite, quartz and Mn and Fe-oxide minerals cut through the

376 underlying sandstone beds (Supplementary Fig. 4).

377   Sandstone beds are moderately to well-sorted and 5-15 cm thick, and Mn-

378 mineralized lithofacies include plane parallel-laminated sandstone, plane parallel

379 laminated to rippled sandstone, planar cross-bedded sandstone, and massive

380 sandstone. Secondary lithofacies include thinly bedded (1-5 cm thick) greenish

381 glauconite-bearing heterolithic sandstone and thin (< 5 cm thick) white to pale-brown

382 sandy tuff beds interbedded with the other Lithofacies. The sandstone facies host the

383 main economic grade Mn oxide ores in the CVSB, which typically construct

384 texturally diverse cements associated with a variety of volcaniclastic detritus (i.e., K-

385   feldspar, lithic fragments, altered volcanic glass, quartz, sericitized plagioclase,

386   chloritized biotite) and authigenic barite and or glauconite. This constitutes part of a

387   separate study devoted to the Mn ores and will not be dealt with further here, as the

388   focus of the current study is on the IFs. Kilias (2011), however, suggested that many

389   of the sedimentary structures identified within the Mn–mineralized sandstone

390   lithofacies are associated with microbial mat growth.

391   The NFIF is composed of strongly banded Fe-rich rocks (Fig. 7) exposed on

392   the topmost part of "Magnus Hill". About 2-3 m thick, the NFIF consists of mm to

393   sub-mm thick, dark grey and brown Fe-rich bands, interbanded with reddish brown

394   Si-rich layers (Figs 7 & 9-11; Supplementary Figs 10-11).   Sedimentary structures in

395   the NFIF are predominantly characterized by rhythmic mm to sub-mm thick bedding

396   (e.g., Fig. 7). The iron oxide-rich bands made up mainly of hematite (Table 1 & Fig.

397   10C) are typically composed of very fine-grained angular to sub-angular volcanic dust

398   material (i.e., fine volcanic ash with particle size under 0.063 mm, K-feldspar,

399   tridymite and cristobalite (Table 1) in an amorphous Si and crystalline hematite

400   matrix (Fig. 12). The predominantly amorphous Si-rich bands are typically planer,

401   finely laminated and composed of microcrystalline to cryptocrystalline ferruginous

402   chert.

403   The NFIF is directly overlain by a   ~1 m thick laminated to massive well-

404   indurated, nodular-pisolitic ironstone bed (Fig. 8A, C & D) that locally preserves a

405   sub-horizontal fabric reflecting the bedding in the original sediment or contain various

406   ferruginous clasts such as fragments, nodules, pisoliths, and ooliths set in a hematite-

407   rich siliceous matrix (Fig. 8C). Scattered cm-scale pisoliths display a crude concentric

408   internal layering, characterized by open and vermiform voids filled by cauliflower-

409   like Mn oxides overprint (Fig. 8D).

410

3.2.1 Interpretation of Section B

412 We interpret the ferruginous NFIF lithofacies to represent the deepest water deposits

413 in the "Magnus Hill" section based on its very fine-grained sedimentary composition,

414 fine laminations and a paucity of intraclast breccias (e.g., Trower and Lowe, 2016,

415 and references therein). These combined with the lack of evidence for wave and

416 current-formed sedimentary structures (e.g., hummocky cross-stratification, trough,

417 ripple cross-stratification, and erosional contacts), indicate quiet water low energy

418 sedimentation, below a likely fair-weather wave base (Simonson and Hassler, 1996;

419 Trendall, 2002; Krapež et al., 2003; Trower and Lowe, 2016; Konhauser et al., 2017).

420 This interpretation is consistent with (1) up section lithofacies change from

421 predominantly sandstone facies of the lower unit to conglomerate facies (Fig. 8B),

422 probably related to a series of channel deposits in an inner-turbidite fan-like setting

423 (Orme and Laskowski, 2016). This sedimentary sequence shows overall deepening

424 from a tidal to shoreface zone depositional environment to an offshore zone during

425 periods of high sea level stand (Trower and Lowe, 2016); (2) conclusions of previous

426 workers suggest that lithofacies with Fe-rich composition similar to the NFIF, were

427 deposited from seawater in a basinal settings (Lowe and Byerly, 1999; Tice and

428 Lowe, 2006). The hypothesized deepening of the "Magnus Hill" section is generally

429 consistent with the interpretation that active rifting was occurring during the filling of

430 the CVSB (Papanikolaou et al., 1990; Stewart and McPhie, 2006; Liakopoulos et al.,

431 2001; Papavassileiou et al., 2017), resulting in the transition from a relatively shallow

432 and deeper water setting represented by the sandstone and conglomeratic deposits, to

433 a relatively deeper quiet water environment, characterized by the finely laminated

434 NFIF facies (Trower and Lowe, 2016).

435   Sedimentary structures and microbial mat fabrics (Kilias et al., 2011) in

436   lithostratigraphic unit A are interpreted to record a variation between storm-

437   dominated shallow-marine (lower shoreface), stable shallow-marine environment

438   with low sedimentation rate in an upper to middle shoreface, and tide-influenced

439   environments (e.g. Noffke et al., 2003; Ramos et al. 2006; Kilias, 2011; Ossa et al.,

440   2016).

441   We interpret that each graded Fe oxide-rich band of the NFIF (Supplementary

442   Figs 8 & 9), represents an individual fallout deposit from a proximal pyroclastic

443   eruption (Stiegler et al., 2011; Trower and Lowe, 2016). This interpretation is

444   supported by normal grading in fine volcanic ash content that reflects their likely

445   origin as pyroclastic fallout deposits in an otherwise quiet water setting (Lowe, 1999).

446   For example, tridymite is a stable SiO_2 polymorph formed at low pressures of up to

447   0.4 GPa and at temperatures of ~870-1470 $^{\circ}$C (Swamy et al., 1994; Koike et al., 2013;

448   Morris et al., 2016). The coincidence of trimydite formation with silicic volcanism is

449   in agreement with the widespread distribution of andesite, dacitite and rhyolitic lava

450   domes in the CVSB. For example, vapour phase production of tridymite together with

451   sanidine identified in this study (Fig. 10) and iron oxides is principally associated

452   with rhyolite ash flow (Breitkreuz, 2013; Galan et al., 2013). Similarly, Cristobalite is

453   a SiO_2 polymorph associated with high temperature rhyolitic eruptions (Horwell et al.,

454   2010). Finally, in situ carbonaceous laminations are absent, suggesting that benthic

455   microbial mat growth had no influence on deposition of the NFIF (Trower and Lowe,

456   2016). Ironstones overlying the NFIF are difficult to interpret with the existing data,

457   but may represent primary granular iron formations (GIF); i.e., a facies transition

458   from BIF-style to GIF-style IF (e.g., Bekker et al., 2010), or supergene ferruginous

459   duricrust formation resulting from subaerial weathering (Anand et al., 2002).

460

3.3 Geochemistry

462 The SEM-EDS-electron micrographs of the NFIF thin sections reveal distinct Fe and

463 Si-rich layers alternating periodically with each other in a fine sediment matrix as

464 shown by the grain size (Figs 9 & 11 & Supplementary Figs 9-11). Laser ablation

465 ICP-MS line analysis indicates Si and Fe count intensities in the Milos BIF-type are

466 comparable to the 2.5 Ga Precambrian BIF reference from the Kuruman IF formation,

467 Transvaal Supergroup, South Africa (Fig. 11). The laser ablation ICP-MS data further

468 show that dramatic fluctuations in Fe concentrations control the Si to Fe ratio in both

469 types of rocks, despite the thousands of millions of years gap between them.

470 No other Fe(III)(oxyhydr)oxide minerals have been identified in the Cape Vani

471 Fe-rich facies different from hematite. Electron imaging of the NFIF Fe-rich bands

472 suggests Si, Al and K-rich phases are mostly associated with the volcaniclastic

473 material predominated by K-feldspar clasts (Fig. 9; Supplementary Figs 10 & 11). A

474 unique feature of the NFIF is that the hematite in the Fe-rich bands occurs in tight

475 association with a carbonaceous material (Fig. 10C), but not for the hematite in the

476 Fe-rich sandstones and in the MFIF. This is also the case for the CIF overlying the

477 MFIF. Hematite showing a fluffy texture and at times presenting as framboidal

478 particles, is sprinkled in the Si-rich cement containing traces of Al and K in the MFIF

479 rocks (Fig. 3). Lack of association of the framboidal-iron-rich particles with S,

480 following SEM-EDS analysis, rules out a pyrite affiliation. This is consistent with the

481 non-sulfidic conditions proposed for the deposition of the Milos BIF-type rocks, as

482 are their Precambrian predecessors. TEM analysis suggests platy nano-Fe oxide-rich

483 particles predominate in the NFIF and MFIF, confirmed by overlaid X-ray Energy

484 Dispersive spectra taken from selected areas (Fig. 12) and consistent with the XRD

485   data showing hematite in both samples. The platy hematite needles in the Milos BIF-

486   type rocks are morphologically, and by size, comparable to hematite needles reported

487   in the ~2.5 Ga Kuruman BIFs (Sun et al., 2015).

488   Unlike the iron-rich bands, volcaniclasts in the Si-rich bands are much smaller

489   in size, occurring mainly as fine-grained (Supplementary Fig. 8-11), signifying

490   predominant precipitation during periods of weaken hydrothermal activity. The SiO_2

491   matrix in both the MFIF are fine-grained, occurring mainly as amorphous opal in the

492   NFIF and crystalline quartz in the MFIF (Figs 10B & 12A-B), while in the MFIF it is

493   mainly present as crystalline quartz (Fig. 12C-D). Relative concentrations of Al, K

494   and Ti in the samples are generally low, with bulk-measured concentrations in both

495   the Si-/Fe-rich bands, together with the SiO_2 and Fe_2O_3 content, strongly covaring

496   with continental crust concentrations (Fig. 13A). Mn impregnation of the MFIF,

497   preserved in the form of replacement layers mostly identified as cryptomelane

498   [$K(Mn^{4+},Mn^{2+})_8O_{16}$) (Table 1), is below detection in the NFIF. Rare hausmannite

499   ($Mn^{2+}Mn^{3+}_2O_4$) was detected in a few cases in the MFIF (Fig. 10D).

500   Trends of major elements from which CIA indices were calculated (Fig. 13B),

501   covary with those of the continental crust (Fig. 13A). Continental crust averages, refer

502   to the zone from the upper continental crust to the boundary with the mantle (Rudnick

503   & Gao, 2003). The calculated CIA indices average 52 with one outlier at 22 (Fig.

504   13B). No distinct relationship could be established between the CIA indices and the

505   respective IFs or between the distinct alternating Si- and Fe-rich bands (Fig. 13).

506   Highly weathered clay minerals resulting from the chemical decomposition of

507   volcanic rocks, e.g., kaolinite representing maximum CIA values of 100 or 75-90 for

508   illite, are absent in the analyzed materials. The absence of carbonates in the rocks

509   strengthened the CIA indices, since CIA indices are expected to be lower when Ca

510   carbonates are present (Bahlburg and Dobrzinski, 2011). TiO_2 content—a detrital

511   proxy—is mostly constant and covaries with the CIA values (Fig. 13B), suggesting

512   little variability and limited continental weathering input. A fairly strong negative

513   linear correlation was found between SiO_2 and Fe_2O_3 values normalized to TiO_2

514   (inset, Fig. 13B).

515   Shale-normalized REE values ($REE_{(SN)}$) for both the MFIF and NFIF are

516   consistent with previous reports (Chi Fru et al., 2013, 2015), and show patterns

517   typical of marine sedimentary environments affected by hydrothermal activity

518   throughout Earth's history (e.g., Planavsky et al., 2010). There is a notable absence of

519   significant negative $Ce_{(SN)}$ anomaly for both the MFIF and NFIF (Fig. 14A-B). These

520   observations are statistically corroborated by true Ce anomalies, calculated as Ce/Ce*

521   ($Ce_{(SN)}/0.5Pr_{(SN)} + 0.5La_{(SN)}$) and Pr/Pr* ($Pr_{(SN)}/0.5Ce_{(SN)} + 0.5Nd_{(SN)}$) and considered

522   significant when Ce/Ce* and Pr/Pr*are less than and greater than 1, respectively (Bau

523   et al., 1996; Planavsky et al., 2010) (Fig. 14B). Further, the Eu/Eu* anomalies

524   averages for the MFIF and NFIF and the distinct Fe-/Si-rich bands, suggest a ~2×

525   higher Eu/Eu* signal for the Si-rich bands relative to the Fe-rich bands and between

526   the MFIF and NFIF deposits (Fig. 14C). Average Pr and Yb shale normalized ratios

527   (Pr/Yb*)—a light vs. heavy REE enrichment proxy (Planavsky et al., 2010)—indicate

528   similar enrichment levels of light and heavy REE in both the NFIF and MFIF, as well

529   as in the Fe- and Si-rich bands (Fig. 14C).

530

531   3.4 Lipid biomarker distribution and chemotaxonomy

532   Bulk $\delta^{13}C_{org}$ averaged −25.4‰ (SD:±0.22), −25.2‰ (±0.26) NFIF Fe-/Si-rich bands

533   and −25.6‰ (SD:±0.12) for bulk MFIF, respectively (Table 2). A fractionation effect

534   between the alternating Fe-/Si-rich layers ($\Delta^{13}C_{\text{Fe-rich NFIF-Si-rich NFIF}}$) is estimated to be

Solid Earth
Discussions

535   ~0.23‰ (SD±0.036), while $\Delta^{13}C_{\text{Fe-rich NFIF-MFIF}}$ and $\Delta^{13}C_{\text{Si-rich NFIF-bulk MFIF}}$, is 0.13‰

536   (SD:±0.11) and 0.36‰ (SD:±0.14), respectively. These differences are small and

537   within the margin of error of analysis, suggesting no strong distinction in $\delta^{13}C_{\text{org}}$

538   preserved in the different IFs and their various facies. They are interpreted to mean

539   similar carbon fixation processes operated during intervals of predominant Si and

540   Fe(III)(oxyhydr)oxides deposition in both IFs. Attempts to discriminate between these

541   environments by lipid biomarker analysis revealed mainly C_{16}-C_{19} fatty acid methyl

542   esters (FAME) in the Fe-rich NFIF bands and in bulk MFIF, while the Si-rich NFIF

543   bands contain mainly C_{12}-C_{21} FAMEs, suggesting either selective preservation (lipid

544   recovery was lower in the Fe-rich MFIF bands) or shifts to different potential

545   biological populations during the deposition of the different layers. Preserved lipids

546   discriminate against typical microbial lipid biomarkers like hopanoids, while C3 plant

547   FAME are detected in all studied materials (Fig. 15). The anaerobic bacteria indicator,

548    $10MeC_{16:0}$ FAME, was however identified in a few bands.

549

550   **4 Discussion**

551   **4.1 Sedimentological processes**

552   The three sub-basin interpretation of the CVSB is consistent with previous proposals

553   suggesting that sedimentation within the CVSB was characterized by active

554   synvolcanic rifting which must have been important in shaping basin topography and

555   the creation of sub-basin architecture (Papanikolaou et al., 1990; Stewart and McPhie,

556   2006; Liakopoulos et al., 2001; Papavassiliou et al., 2017). Moreover, this tectonic

557   regime would suggest that the location(s) of volcanism were continually changing

558   relative to the two stratigraphic sections, which themselves were also being affected,

559   i.e. changes in depositional water depth and sedimentation style or and/or that local

560 submarine or subaerial topographic highs impeded the lateral continuity of

561 sedimentary units (Stewart and McPhie, 2006; Trower and Lowe, 2016). Chi Fru et al.

562 (2015) have suggested there is an upward deepening of the overall depositional

563 setting recorded in the "Little Vani" section, consistent with rifting during CVSB

564 infilling time.

565   The CVSB floored by dacitic/andesitic lava domes and overlain by

566 vocaniclastic infill, dates back to Upper Pliocene-Lower Pleistocene. A complex

567 mosaic of lithologically diverse sedimentary units (blocks), confined by neotectonic

568 marginal faults, characterizes the CVSB (Fig. 2). The most pronounced of these faults

569 being the NW-trending Vromolimni-Kondaros fault (Papanikolaou et al., 1990) that

570 has been proposed as the trigger of the hydrothermal activity that deposited Mn ore in

571 the CVSB (Papanikolaou et al., 1990; Liakopoulos et al., 2001; Alfieris et al., 2013;

572 Papavassiliou et al., 2017). The stratigraphically tight coupling between Mn and Fe

573 deposition, linked by Fe oxide minerals in feeder-veins, and positive Eu anomalies

574 (Fig. 14) indicating vent-sourced Fe (Maynard, 2010), associate Fe mineralization to

575 fault-triggered hydrothermalism in the CVSB. This is consistent with models of

576 geothermal fluid circulation along fault lines as conduits for the Mn-rich fluids that

577 formed the Milos Mn ore deposit (Hein et al., 2000; Liakopoulos et al., 2001; Glasby

578 et al., 2005; Kilias, 2012; Papavassiliou et al., 2017). More importantly, the overall

579 complex neotectonic structure of the CVSB (Papanikolaou et al., 1990) would explain

580 the creation of restricted basins, with sedimentological, lithological and geothermal

581 conditions that enabled the development of unique biogeochemical circumstances in

582 which the NFIF and MFIF formed.

583   The presence of the three depositional basins is supported by the fact that the

584 sequence lithologies in each fault-bound unit are characterized exclusively by

585   occurrences of specific and variably thick stratigraphic packages that tend to be

586   absent in others. For example, the MFIF occurs restricted to basin 1 and the NFIF to

587   Basin 3. Basin 2 is further distinguished by 35-50 m thick interbedded ore-grade Mn-

588   mineralized and glauconitic sandstones/sandy tuffs, much less developed in Basins 1

589   and 3 (Fig. 2). The presence or absence of a stratigraphic sequence, together with its

590   thickness variation, are interpreted as a result of local syntectonic sediment formation

591   conditions in each basin as a result of block tectonic movements along fault lines

592   (Papanikolaou et al., 1990; Nijman et al., 1998). It may also be attributed to unique

593   basin scale water column redox conditions (e.g. Bekker et al., 2010, and references

594   therein), post-depositional erosion and changing sea level stand (Cattaneo & Steel,

595   2000).

596   The lack of hydrothermal feeder veins or seafloor exhalative structures (i.e.,

597   chimneys) in the MFIF and NFIF lithologies, suggests that hydrothermal Fe(II) was

598   delivered by diffuse flow and that the Milos-IF formed on the seafloor. Importantly, a

599   number of studies propose that the main Mn deposit in Basin 2 formed in two stages.

600   First boiling hydrothermal fluids precipitated sulfide at depth, leading to first

601   generation microbial-induced deposition of Mn oxides as pyrolusite and ramsdellite.

602   Tectonic uplift resulted in the replacement of the first generation Mn minerals by

603   second-generation Mn oxides, including cryptomelane (Hein et al., 2000;

604   Liakopoulous et al., 2001; Papavassiliou et al., 2017). Cryptomelane replacement of

605   the original Fe(III)(oxyhydr)oxides in MFIF therefore suggests that deposition of the

606   MFIF is coeval with first stage Mn deposition in Basin 2. This observation also

607   indicates that at this time, two active fault-bounded basins probably existed in the

608   CVSB; i.e., Basins 2 and 3 (Fig. 2). For example, the underlying Mn-enriched

609   sandstone lithology in Basin 3, stratigraphically correlated to the sandstone Mn

610 deposit in Basin 1 and the MFIF Fe-Si-rich rocks in Basin 2, justify this proposal (Fig.

611 2).

612 A subsequent geomorphological/chemical reconfiguration formed Basin 3,

613 orchestrating the deposition of the NFIF in a deeper, small-restricted basin (Fig. 2).

614 The deepening of Basin 3 is strongly demonstrated by an underlying fine upward

615 grading of a transgressive-type Fe-rich lag deposit, that transitions into the NFIF. This

616 uplifting into shallower water event that prompted second generation deposition of

617 Mn oxides in Basin 2 and the substitution of Fe(III)(oxyhydr)oxides by Mn in sub-

618 Basin 1, potentially triggered this environmental change in Basin 3. The MFIF and

619 NFIF sequences are therefore temporally and spatially distinct (Fig. 2).

620

621 **4.2 Formation Mechanism of The Milos BIFS**

622 **4.2.1 Paragenetic sequence**

623 It is stressed that the previously generalized model proposed for biological deposition

624 of the Milos IF, refers exclusively to parts of what is now designated as MFIF (Chi

625 Fru et al., 2013). The NFIF is strongly banded, but does not display the typical

626 microfossils seen in the MFIF, where diffused microbanding apparently relates to the

627 distribution of microbial mats in thin sections (Chi Fru et al., 2013, 2015). The

628 distinction of microcrystalline quartz and amorphous silica phases in the MFIF and

629 NFIF, respectively, together with nano-crystalline hematite particles, suggests a

630 primary amorphous silica origin in both deposits, diagenetically transformed to quartz

631 in the MFIF. The difference in silica crystallinity between the IFs is concurrent with

632 the older age predicted for the MFIF relative to the NFIF, from reconstructed

633 sequence stratigraphy (Fig. 2). Hematite in BIFs is generally interpreted, based on

634 thermodynamic stability, to be a transformation of various primary Fe(III) minerals,

Solid Earth
Discussions

635   with ferrihydrite often proposed as the principal precipitate from the water column

636   (Glasby and Schulz, 1999; Bekker et al., 2010; Johnson et al., 2008; Percoits et al.,

637   2009). It is thought that acidic pH yields mainly goethite while hematite is produced

638   at circumneutral pH (Schwertmann and Murad, 2007). The notable absence of

639   diagenetic magnetite and Fe carbonates (siderite and ankerite), point to negligible

640   coupling of primary Fe(III) oxyhydroxides reduction to organic matter oxidation by

641   the dissimilatory iron-reducing bacteria during burial diagenesis (Johnson et al.,

642   2008). Minor occurrence of iron-silicate phases (Chi Fru et al., 2015) indicates an

643   origin of the hematite precursor in seawater independent of the iron silicate proposed

644   in some cases (Fischer and Knoll, 2009; Rasmussen et al., 2013, 2014). The up to 50

645   wt% Fe content recorded in the Fe-rich bands, indicate that large amounts of

646   dissolved Fe(II) was intermittently sourced and deposited as primary Fe(III) minerals,

647   through various oxidative processes in the depositional basin.

648   Importantly, the CIA index does not support mass weathering and

649   mineralization of terrestrial Fe and Si, in agreement with the absence of rivers

650   draining into the CVSB (Chi Fru et al., 2013). The specific identification of plant

651   biolipids would at face value imply post-depositional contamination. However,

652   samples were sawn to remove exposed layers and only the laminated bands for the

653   NFIF were analyzed, while modern sediments from Spathi bay, located Southeast of

654   Milos Island where hydrothermal activity is presently ensuing at 12.5 m below sea

655   level, revealed similar plant lipids as recorded in the Quaternary IF (Fig. 15G). Post-

656   depositional contamination with terrestrial plant lipids is therefore ruled out for the

657   idea that recalcitrant plant biomass probably entered the sediments via seawater

658   entrainment at the time of deposition (see Naden et al., 2005). This finding

659   necessitates the careful interpretation of bulk $\delta^{13}C_{org}$ values obtained from both the

660   modern and ancient Milos sediments, involving in situ and ex situ biological

661   contributions to $^{13}C_{org}$ fractionation by various known carbon fixation pathways

662   (Preuß et al., 1989; Berg et al., 2010).

663   Such indication of mixing of the hydrothermal fluids with seawater may be

664   interpreted to negate a reducing depositional environment as suggested by the Ce

665   anomalies. However, Pichler & Veizer (1999) demonstrated that in the unconfined

666   seafloor shallow hydrothermal vent fields at Tatum Bay, Papua New Guinea,

667   experiencing little or no water column stratification, as low as 11% seawater is

668   involved in the precipitation of Fe(III)(oxyhydr)oxides from hydrothermal fluids and

669   at maximum 57%. It is therefore suggested that seawater mixing during deposition

670   was at the lower limits. This is demonstrated by the REE analysis and the presence of

671   anaerobic bacteria biomarkers in the NFIF formation, coupled to sediment lithology

672   and stratigraphy, as explained below.

673

674   **4.2.2 Tectono-sedimentary processes and band formation**

675   Fluctuation in hydrothermal activity is proposed to account for the banding in the

676   NFIF (Fig. 16), under redox depositional conditions inferred to be mainly reducing

677   for both investigated IFs, consistent with previous reports (Chi Fru et al., 2013, 2015).

678   Positive Eu anomalies indicate a hydrothermal origin for all but one of the sample

679   suite (Fig. 14A). However, statistically calculated Eu/Eu* anomalies ($Eu_{(SN)}$/

680    $(0.66Sm_{(SN)} + 0.33Tb_{(SN)})$) to correct for differences in Gd anomalies commonly

681   encountered in seawater (Planavsky et al., 2010) are in the range of 0.1-0.58,

682   averaging 0.42. The values are closer to the anoxic water column values calculated for

683   Archean IFs, compared to Paleoproterozoic IFs (Planavsky et al., 2010), which may

684   be due to their deposition in an active volcanic center like most of the Archean

685   Agloma BIFs (Bekker et al., 2010; Chi Fru et al., 2015). The lack of statistically

686   significant true negative Ce anomalies (Fig. 14B) is interpreted to indicate a reducing

687   depositional environment for both IFs.

688   CIA indices traditionally provide relative information on contributions from

689   chemical weathering to sediment deposition, linked to operative hydrological and

690   climatological patterns on land. This information is often gleaned from ancient and

691   modern soils and from reworked siliclastic deposits in marine basins (Maynard, 1993;

692   Bahlburg & Dobrzinski, 2011). The calculated CIA indices, however, are closer to the

693   range obtained for unweathered and or only minimally weathered volcanic rocks (e.g.,

694   Nesbitt & Young, 1982; Bahlburg & Dobrzinski, 2011), thus pointing to a

695   predominantly volcanic and/or hydrothermal provenance for the clastic sedimentary

696   materials in the IFs (also see Alfieris et al., 2013).

697   It has been suggested that the release of reduced submarine hydrothermal fluids

698   contributed towards maintaining water column anoxia during the deposition of

699   Precambrian BIFs (Bekker et al., 2010). The calculated Eu anomalies (Fig. 14) and

700   petrographic data showing volcaniclastic detritus (i.e., K-feldspar, sanidine, tridymite,

701   cristobalite) as key rock components are in agreement with a submarine hydrothermal

702   source for the investigated IFs. The coarse volcaniclastic detritus embedded in the Fe-

703   rich bands compared to the finer particles in the Si-rich layers, highlights rapid

704   oxidation of Fe(II) that coincided with periodic cycles of hydrothermal/volcanic

705   discharge of new materials into the water column. However, the fine-grained nature

706   of both the MFIF and NFIF deposits suggests that deposition likely occurred away

707   from where such activity was occurring or that volcanic/hydrothermal discharge of Fe

708   and Si was non-eruptive and disruptive. The Fe-rich bands repetitively revealed

709   hematite grains cementing the denser volcaniclastic fragments that gradually diminish

Solid Earth
Discussions

Open Access

EGU

710   upwards into a zone of fine-grained hematite before transitioning into Si-rich bands

711   consisting mainly of finer volcaniclastic detritus. These observations provide four

712   valuable interpretational considerations for proposing a model for the formation of the

713   alternating Si and Fe-rich bands.

714   1. The Si and Fe oxides-rich bands are a primary precipitate formed in the water

715   column, by a process in which the precipitation of amorphous Si occurred

716   during quiescent non-volcanic intervals, after the oxidation and precipitation

717   of reduced Fe intermittently introduced into the water column by

718   volcanic/hydrothermal activity to form the Fe oxides.

719   2. The repetitive zonation of distinct particle sizes, suggests density gradient

720   sedimentation that requires a water column-like environment, rather than

721   diagenetic alteration of pre-formed sediments by hydrothermal fluids.

722   3. The lack of statistically significant Ce anomaly across the Si and Fe-rich units

723   does not support sediment diagenesis as an alternative model for explaining

724   the origin of the Milos IF, in favor for a primary water column source. This is

725   because the oxidation of ferrous Fe supplied by reduced hydrothermal fluids

726   to iron oxides, requires coincidental interaction with a sizeable pool of

727   oxygen (Johnson et al., 2008). Otherwise, light-controlled photoferrotrophy—

728   an extremely rare sediment characteristic—precipitates Fe oxides in the

729   absence of oxygen (Weber et al., 2006).

730   4. The style of deposition of the MFIF and NFIF is distinct from the post-

731   depositional infilling of a porous sandstone sediment matrix during the

732   formation of the Mn ores. Instead the deposition of the MFIF and NFIF in

733   restricted portions in the basins not associated with previously accumulated

734   sandstones, and the difficulty and lack of evidence to provide a viable

Solid Earth
Discussions

735   biogeochemical mechanism for the formation of the even bands of alternating

736   Si and Fe-rich layers of several meters high and wide, does not support post-

737   depositional pore filling of a porous sandstone matrix by Fe, as a potential

738   pathway to the formation of the Milos IF.

739

740   **4.2.3 Biological involvement**

741 Hematite precipitation in the MFIF on microbial filaments (Chi Fru et al., 2013) was

742 previously used to propose a generalized basin-scale mechanism for the deposition of

743 Fe-rich rocks in Cape Vani. However such filaments are absent in the NFIF, while

744 pure hematite grains are tightly bound to relics of an organic matter signal carrying a

745 maximum $\delta^{13}C_{org}$ signature of -25‰ (Table 2). Similar processes are recorded in

746 modern marine sediments where interactions between Fe and free organic matter has

747 been reported to enable the preservation up to 21.5wt% of total organic carbon over

748 geological time scales (Lalonde et al., 2012). Moreover, Fe generally traps and

749 preserves organic matter at redox interfaces (Riedel et al., 2013)**.** The data appear to

750 suggest that the mechanism of Fe(III) (oxyhydr)oxide precipitation and preservation

751 varied between the two IFs. The lack of similar photoferrotrophic-like filamentous

752 fossils reported in the MFIF (Chi Fru et al., 2013), in the NFIF, does not however rule

753 out the potential role of microbial involvement in Fe(II) oxidation, since diverse

754 microbial taxa carry out this process, several of which are non-filamentous (Chi Fru et

755 al., 2012). However, our data is insufficient to enable clear quantification of the levels

756 of abiotic vs. biotic contribution to Fe(II) oxidation in the NFIF. Nevertheless, the

757 inferred predominantly anoxic depositional conditions as explained above, together

758 with the identification of anaerobic bacteria biomarkers in the laminated bands,

759 intuitively favor significant contribution of anaerobic biological Fe(II) oxidation in

760 the precipitation of primary Fe(III)(oxyhydr)oxides in the NFIF. See Weber et al.,

761 2006, for a review of potential biological pathways to anaerobic Fe(II) oxidation.

762   Briefly, anaerobic microbial Fe(II) oxidation can proceed via nitrate reduction

763 and by photoferrotrophy to deposit Fe(III)(oxyhydr)oxides. These mechanisms have

764 been linked to microbial contribution to BIF formation (Weber et al., 2006; Kappler et

765 al., 2005) and also for the MFIF (Chi Fru et al., 2013). However, it is also possible

766 that microaerophilic neutrophilic Fe(II)-oxidizing bacteria likely played an important

767 role, assuming a depositional setting analogous to the Santorini caldera and Kolumbo

768 shallow submarine volcanoes, where such low-O_2-dependent microbial Fe(II)

769 oxidation has been identified to actively precipitate Fe(III) (oxyhydr)oxides (Kilias et

770 al., 2013; Camilli et al., 2015). It appears that in the MFIF, precipitating

771 Fe(III)(oxyhydr)oxide minerals were bound and preserved free of organic carbon or

772 that such organic carbon was diagenetically degraded. As was previously shown,

773 Fe(III)(oxyhydr)oxides completely replaced the organic content of the filamentous

774 microfossils in the MFIF (Chi Fru et al., 2013).

775   The 10MeC$_{16:0}$ FAME identified in the rocks has been reported in anaerobic

776 organisms coupling nitrite reduction to methane oxidation (Kool et al., 2012), in

777 sulfate and iron-reducing bacterial species such as Desulfobacter, Desulfobacula

778 (Bühring et al., 2005; Dowling et al., 1986; Taylor and Parkes, 1983), Geobacter,

779 Marinobacter and the marine denitrifier, Pseudomonas nautical (Kool et al., 2006;

780 Bühring et al., 2005; Dowling et al., 1986). It had previously been proposed that post-

781 depositional denitrification was a potential pathway for early organic matter removal,

782 justified by the low rock organic carbon and nitrogen content in the Milos BIF-type

783 rocks (Chi Fru et al., 2013, 2015; Table 2). Equally, the detected 10MeC$_{16:0}$ FAME

784 has also been found in anaerobic oxidation of methane (AOM) communities (Alain et

785   al., 2006; Blumenberg et al., 2004), originating from sulfate reducing bacteria.

786   However, bulk sediment $\delta^{13}C_{org}$ of $-20‰$ does not reflect AOM activity that is

787   expected to produce bulk $\delta^{13}C_{org}$ values that are $\leq-30‰$. Low $10MeC_{16:0}$ FAME

788   concentrations frustrated attempts at acquiring its compound specific isotopic

789   signature to enable further biomolecular level reconstruction of active microbial

790   metabolisms to explain Fe deposition mechanisms.

791   It is nevertheless puzzling why potential microbial biomarkers typical of marine

792   or hydrothermal vent environments are hardly preserved in the rocks, given that

793   microfossil evidence indicates a vast community of diverse prokaryotic assemblages

794   in the adjacent MFIF (Chi Fru et al., 2013, 2015). Moreover, sediments of the modern

795   Milos hydrothermal system and elsewhere on the HVA, are ubiquitously colonized by

796   microbial life, characterized by the marked large-scale absence or low abundance of

797   higher life forms, including plants (Kilias et al., 2013; Camilli et al., 2015; Oulas et

798   al., 2015). One possibility could be the discriminatory preservation of lipids related to

799   their selectivity and reactivity towards Fe(III)(oxyhydr)oxides and clays or different

800   pathways to diagenetic degradation (e.g., Canuel & Martens, 1996; Lü et al., 2010;

801   Riedel et al., 2013). As noted, the carbonaceous materials in the BIF-type NFIF rocks

802   occur in tight association with hematite.

803   Importantly, prokaryotic biomarkers are suggested to poorly preserve in these

804   young BIF analogues. This raises the possibility that this may provide an important

805   explanation for why lipid biomarkers are yet to be extracted from Precambrian BIFs.

806   Moreover, the data are compatible with low C_{org} recorded in BIFs of all ages. They

807   suggest these unique BIF features may not be entirely related to metamorphic

808   degradation of organic matter, since the Milos BIF-type rocks are unmetamorphosed,

809   yet have vanishing C_{org} levels similar to the ancient metamorphosed BIFs.

810

4.2.4 Mn layers and the deposition of the Si-Fe-rich facies

812 Cryptomelane [$K(Mn^{4+},Mn^{2+})_8O_{16}$], commonly occurring in oxidized manganese

813 deposits resulting from mineral replacements and as open space fillings

814 (Papavassiliou et al., 2016), common in MFIF, supports the idea of post-depositional

815 impregnation of the base of the MFIF by Mn-rich fluids. Microscopic analysis

816 supports the epigenetic origin of the Mn in the MFIF by revealing Mn oxides growing

817 along fractures, impregnating and replacing Fe minerals (Fig. 4B-F). The

818 macroscopically evident thinning out to disappearance of such Mn-rich horizons up

819 the MFIF, coupled by their development along microfractures emphasizes this

820 epigenetic Mn origin. Mn is not a common feature of the NFIF, even though it sits on

821 top of a thin sandstone layer impregnated by Mn, that locally forms the cap of the

822 main Mn ore at Cape Vani. The generally accepted view is that Mn rich hydrothermal

823 fluids rose and mineralized the Cape Vani sandstones (Hein et al., 2000; Liakopoulos

824 et al., 2001; Glasby et al., 2005). Based on the stratigraphic location of the MFIF

825 which pre-dates the Mn-rich sandstones, it is proposed that impregnation of the MFIF

826 by Mn was coeval with large-scale Mn ore mineralization of the Cape Vani

827 sandstones, implying the entire basin was likely oxygenated at the time. The lack of

828 Ce anomalies suggests that both the MFIF and the NFIF formed in anoxic settings.

829 Similar data for the Mn oxides have suggested formation in oxic settings (Glasby et

830 al., 2005; Chi Fru et al., 2015). However, more sensitive proxies are needed to resolve

831 and confirm the stratigraphic and REEs-dependent interpretation of potential redox

832 conditions. This implies that Mn epigenetically replaced the MFIF, either because the

833 basin was tectonically uplifted into a high–energy oxygenated shallow water setting

834 or that sea level dropped, leading to partial metasomatism of the base of MFIF, when

835   oxygenated seawater mixed with hydrothermal fluids and precipitated Mn. The lack

836   of significant Ce anomalies in the dataset also indicates that for the final deposition of

837   the NFIF, an eventual deepening event or sea level rise, or both, were tectonically

838   triggered, resulting in deoxygenation of parts of the CVSB.

839   All of this is feasible with the three-basin-fault-bounded hypothesis as a

840   requirement for movement along fault lines in response to temporal tectonic

841   activation. Importantly, a deepening event is suggested by the sudden change from the

842   underlying Mn-rich layer into the conglomeratic deposit (Fig. 8B) often associated

843   with sedimentary features that form during sea level rise and the landward migration

844   of the shoreline (Cattaneo & Steel, 2000). The upward sequential transition from the

845   Mn-rich facies through pebbly to fine-grained sediment to the NFIF, strongly implies

846   that the underlying Mn-rich facies and NFIF layers formed in shallower and deeper

847   waters, respectively, or that they are separated by an erosional unconformity. This

848   study proposes that the NFIF that overlies the transgressive-type conglomeratic lag

849   along an erosional contact surface was likely deposited during maximum flooding,

850   when the basin became stagnant and stratified, and subsequently was uplifted to

851   emergence. Similar transgression-type lithologies are indicated to have regulated

852   primary sedimentation styles during the deposition of nearshore Paleoproterozoic

853   BIFs (Pufahl and Fralick, 2004; Pufahl et al., 2014). Moreover, deposition of BIFs in

854   sandstone/grainstone-dominated environments has also been suggested for

855   Precambrian IFs (Simonson, 1985; Simonson and Goode, 1989; Pufahl and Fralick,

856   2004).

857   Uplifting is suggested by potential the weathering of the NFIF to form the

858   ferruginous duricrust cap. Comparable ferruginous layers on Precambrian BIFs are

859   linked to pervasive subaerial chemical weathering, via the dissolution of the silica-

860   rich layers and precipitation of relatively stable Fe oxides in the spaces between more

861   resistant hematite crystals (e.g., Dorr, 1964; Shuster et al., 2012; Levett et al., 2016).

862   This collective evidence supports the existence of a geodynamic tectonic system

863   capable of producing shallow oxic to deeper anoxic basin conditions at different times

864   that would explain the existence of Mn and Fe oxide layers within the same

865   sedimentary sequence. For example, it is common knowledge that both Fe and Mn

866   oxides will precipitate in the presence of oxygen (Roy, 1997, 2006), with kinetic rates

867   usually being faster for the oxidation of reduced Fe than reduced Mn. In the Fe(II)-

868   rich conditions that prevail in anoxic settings, abiotic reactions between Fe(II) and Mn

869   oxides, produce Fe(III) leading to the dissolution of the Mn oxides to form reduced

870   Mn, implying Mn oxides should not accumulate (Dieke, 1985). Moreover, under these

871   conditions, biological precipitation of Fe(III) can occur rapidly, leaving dissolved Mn

872   in solution to be deposited when oxygen becomes available. Given that the

873   hydrothermal fluids of the Hellenic Volcanic Arc are commonly enriched in both

874   reduced Fe and Mn, the deposition of the MFIF and NFIF therefore implies there was

875   an existing mechanism that enabled the kinetic discrimination and deposition of the

876   oxides of Fe and Mn into separate settings, most likely dependent on prevailing redox

877   conditions. The accumulation of the ferruginous duricrust layer, overprinted by redox

878   sensitive Mn-nodules, above the NFIF indicates a new shallowing event might have

879   terminated the formation of the NFIF.

880

881   **4.2.5 Modern analogues on the HVA**

882   Mechanistic explanation for the development of potential stratified waters and

883   reducing conditions during the deposition of the Milos BIF is problematic. However

884   evidence is available from present shallow submarine hydrothermal analogues in the

885   central part of the HVA, to which the CVSB belongs. These include:

886   (1) The crater floor of the Kolumbo shallow-submarine volcano (~600×1200

887   m^3), which rises from 504 to 18 m below sea level near Santorini, (Sigurdsson et al.,

888   2006; Carey et al., 2013; Kilias et al., 2013).

889   (2) The N part of Santorini's submerged caldera walls, which rises from 390 m

890   below sea level to over 300 m above sea level (Druitt et al., 1999; Friedrich et al.,

891   2006; Nomikou et al., 2013; Camilli et al., 2015).

892   (3) The coastal embayments at the Kameni emergent volcanic islands in the

893   centre of the Santorini caldera (Hanert, 2002; Nomikou et al., 2014; Robbins et al.,

894   2016).

895   The benthic waters within Kolumbo's crater potentially sustain O_2 depleted

896   conditions via stable CO_2-induced water column densification, and accumulation of

897   acidic water (pH~5), extending ~10 m above the CO_2 venting crater floor (Kilias et

898   al., 2013). This phenomenon is believed to lead not only to obstruction of vertical

899   mixing of bottom acidic water, but also to O_2 deprivation by precluding efficient

900   transfer of oxygenated surface seawater into the deeper crater layer. In addition,

901   diffuse CO_2 degassing is believed to be linked to the formation of Fe microbial mats

902   and amorphous Fe(III) oxyhydroxides on the entire Kolumbo crater floor (Kilias et

903   al., 2013). Prerequisites for the O_2 depleted conditions to happen are the closed

904   geometry of the Kolumbo crater and the virtually pure CO_2 composition of the

905   released hydrothermal vent fluids that produce oxygen stratification along a stable

906   CO_2-pH gradient.

907   A similar scenario is reported for the Santorini caldera, where large (~5 m

908   diameter) CO_2-rich, acidic (pH, ~5.93) hydrothermal seafloor pools and flow

909   channels, develop within m-thick microbial Fe-mats on the seafloor slope at 250-230

910   m below sea level. Persistent hypoxia exists in these pools, representing concentrated

911   seafloor CO_2 accumulation centers generated by hydrothermal venting (Camilli et al.,

912   2015). Here, the dissolved O_2 content (~80 µM or less) in the pools is ~40 % depleted

913   relative to the surrounding ambient seawater (Camilli et al., 2015). These hypoxic

914   conditions are comparable to or even lower than those measured in the CO_2-rich

915   oxygen minimum zones of coastal oceans, relative to seawater existing in equilibrium

916   with atmospheric pO_2 and pCO_2 pressures (Paulmier et al., 2008, 2011; Franco et al.,

917   2014). These conditions enable strong redox stratification of the pool waters, in which

918   unique Si- and Fe-rich microbial mats are associated with amorphous opal and

919   Fe(III)(oxyhydro)xides (Camilli et al., 2015). Importantly, the Fe microbial mats in

920   these CO_2-rich hypoxic pools are affiliated with specific microaerophilic Fe(II)-

921   oxidizing bacteria that accumulate Fe(III) oxyhydroxides (Camilli et al., 2015; Oulas

922   et al., 2015). These Fe bacteria are implicated in the deposition of the Precambrian

923   BIFs (Konhasuer et al., 2002; Planavsky et al., 2009; Bekker et al., 2010).

924   Hypoxia is also associated with the water column of the Fe(III)-rich coastal

925   embayments and their hydrothermal vents (≤1.0 m water depth), Kameni islands,

926   considered a modern analogue environment for the precipitation of Precambrian BIFs

927   (Hanert, 2002; Robbins et al., 2016 and references therein). Venting fluids are warm

928   (20-40 °C), acidic to circumneutral (pH 5.5-6.9), enriched in CO_2, Fe and Si

929   (Georgalas & Liatsikas, 1936, Böstrom et al., 1990; Handley et al., 2010; Robbins et

930   al., 2016). Water column stratification is expressed as decreasing O_2 with depth that is

931   positively related to Fe(III)(oxyhydr)oxide density and microaerophilic Fe(II)-

932   oxidizing bacterial prevalence (Hanert, 2002). Robbins et al. (2016) found that

933   Fe(III)-rich suspended particulate material in these "Fe bays" may be associated with

934   anoxia, extending up to the air-seawater interface, near the hydrothermal vents

935   (Hanert, 2002). They consist of ferrihydrite, goethite and microaerophilic Fe(II)

936   oxidizers.

937   The biogeochemical occurrence of these phenomena within the localized

938   confines of the Santorini caldera and Kolumbo crater, may however be difficult to

939   achieve in ordinary shallow submarine hydrothermal settings, such as those occurring

940   on the coast of present day Milos. The same may be true for Tatum Bay, where non-

941   volcanic and unconfined diffuse hydrothermalism is widespread (Dando et al., 1996;

942   Pichler & Dix, 1996; Pichler & Veizer, 1999; Stüben et al., 1999; Rancourt et al.,

943   2001; Varnavas et al., 2005).

944   In the Kolumbo and Santorini hydrothermal fields, benthic pH averages 5.5 and

945   the deposition of carbonates is markedly absent (Kilias et al., 2013, Camilli et al.,

946   2015; Robins et al., 2016). This conforms to observations in the MFIF and NFIF units

947   where carbonate mineralization is not detected, thereby suggesting a similar low pH

948   depositional environment for both the MFIF and NFIF. Ubiquitous

949   Fe(III)(oxyhydr)oxide precipitation and enriched Si content are prevalent in the CO_2-

950   rich-hypoxic shallow submarine Santorini caldera slope pools and the Kameni Fe-

951   embayments where sulfide precipitation is inhibited (Camilli et al., 2015), or

952   extremely rare (Robbins et al., 2016). Such sulfide-poor conditions are critical for the

953   formation of BIFs (Bekker et al., 2010). Moreover, the anoxic amorphous Si-

954   Fe(III)(oxyhydr)oxide-rich-sulfide-poor shallow submarine environments at Kameni

955   islands, have been independently proposed as a modern analogue environment for

956   Precambrian BIF precipitation (Hanert, 2002; Robins et al., 2016).

957   A high Si-Fe(III)(oxyhydr)oxide content, absence of carbonate and sulfide

958   mineralization, coupled to a generally low S content have also been demonstrated for

959   the CVSB Fe formations (Chi Fru et al., 2013, 2015). This depositional situation is

960   different, for example, from the unconfined shallow submarine hydrothermal systems

961   in Tatum Bay and Bahia Concepcion Bahia Carlifornia Sur, Mexico, where authigenic

962   carbonate deposition is widespread (Canet et al., 2005; Pichler & Dix, 1996, 2005).

963   Moreover, there is strong geological evidence that within volcanic crater

964   environments associated with high CO_2 emission, long-term water column redox

965   stratification is possible under these special conditions. Further evidence is found in

966   volcanic crater lakes (for example the shallow 205 m deep lake Nyos in Cameroon—

967   renowned as one of Earth's three CO_2 saturated volcanic lakes (Ozawa et al., 2016;

968   Kling et al., 2005)). Here CO_2-induced water column stratification is associated with

969   bottom reducing conditions characterized by a low sulfate and high Fe bottom water

970   content relative to surface concentrations (Tiodjio et al., 2014).

971

972   **5 Concluding remarks**

973   This study shows the following new insights in light of what was previously known:

974   1. At least two distinct IFs (MFIF and NFIF) formed from hydrothermal mud,

975   within two localized sub-basins in the ~1 km-long CVSB, ~2.66-1.0 Myr ago,

976   controlled by local tectonism.

977   2. A working model that band formation may involve potential

978   Fe(III)(oxyhydr)oxide filling of sediment pores and fractures during

979   diagenesis, is not supported by the data. In addition to the lack of observation

980   of such phenomena, as demonstrated for replacive Mn mineralization,

981   calculated Ce and Eu anomalies, together with preliminary sequential iron

982   extraction analysis (Poulton and Canfield, 2011; data not shown), are

983   suggestive of anoxic depositional conditions likely induced by the release of

984   reduced hydrothermal/volcanic fluids into a cutoff sedimentary basin.

985   3. The precipitation of Fe(III) and Mn oxides require oxygen. In the absence of

986   oxygen, Mn is not oxidized, while light and photoferrotrophy will oxidize

987   reduced Fe to Fe(III)(oxyhydr)oxides. Both light and photoferrotrophy are

988   however extremely rare characteristics of anoxic sediments, but a common

989   feature of anoxic Fe^{2+}-rich waters, where photoferrotrophy is widespread

990   (Weber et al., 2006). Collectively, these observations provide an important

991   feasible mechanism for the knife sharp separation of the Mn oxide-rich ores

992   in the CVSB that are also Fe(III)(oxyhydr)oxide-rich, from the highly

993   localized MFIF and NFIF deposits that are Fe(III)(oxyhydr)oxide-rich but Mn

994   oxide-poor.

995   4. The mechanism of formation of the MFIF and NFIF therefore most likely

996   involved exhalative release of reduced hydrothermal/volcanic fluids into a

997   restricted and deoxygenated seafloor water column where the oxidation of

998   reduced Fe to Fe(III)(oxyhydr)oxides occurred, most likely by the activity of

999   photoferrotrophs (Chi Fru et al., 2013).

1000   5. Episodic intensification of hydrothermal activity is identified as a main

1001   mechanism for the formation of the millimetric BIF bands (Fig. 16), adding to

1002   the biological mechanism that was inferred from fossil records in the MFIF

1003   (Chi Fru et al., 2013, 2015).

1004   6. Abiotic Si precipitation was apparently much slower relative to Fe(III)

1005   precipitation, resulting in Fe-rich bands in the NFIF forming in association

1006   with large fragments of volcaniclast and the Si-rich bands with fine Si grains.

1007   7. A combination of the above processes produced pulses of Si and Fe in the

1008   millimetric Si and Fe-rich bands in the NFIF.

1009   8. The Milos rocks fulfill sedimentological, chemical and mineralogical

1010   characteristics that established them as potentially the youngest known BIFs;

1011   following the simplistic definition that BIFs are sedimentary rocks composed

1012   of alternating layers of Fe and Si containing at least 15% iron.

1013   9. Whether the rocks described here are analogues of Precambrian BIFs or not,

1014   and whether the proposed formation mechanisms match those that formed the

1015   ancient rocks, is opened to debate. Nonetheless, the present study provides

1016   mechanisms by which rocks with Fe and Si-rich bands can be formed in the

1017   modern oceans.

1018

1019   *Data availability. Data can be accessed by request from any of the authors*

1020

1021   *Author contributions.* ECF, SK and MI designed the study. ECF, SK, KG and MI

1022   performed fieldwork. ECF, JER, KG, IM and QH performed research. ECF, SK, KG,

1023   IM, QH and JER interpreted data. ECF and SK wrote paper.

1024

1025   *Competing interests.* The authors declare that they have no conflict of interest.

1026

1032 **References**

1033 Alain, K., Holler, T., Musat, F., Elvert, M., Treude, T., and Kruger M.;

1034   Microbiological investigation of methane- and hydrocarbon-discharging mud

1035   volcanoes in the Carpathian Mountains, Romania. Environ. Microbiol., 8, 574–

1036   590, 2006.

1037 Alfieris, D. and Voudouris, P.: Ore mineralogy of transitional submarine magnatic-

1038   hydrothermal deposits in W. Milos Island, Greece. Bul. Acad. Sci., 43, 1–6, 2005.

1039 Alfieris, D.; Geological, geochemical and mineralogical studies of shallow submarine

1040   epithermal mineralization in an emergent volcanic edifice, at Milos Island (western

1041   side), Greece. PhD thesis, Department Geowissenschaften der Universität

1042   Hamburg, 2006.

1043 Alfieris, D., Voudouris, P., and Spry, P.: Shallow submarine epithermal Pb–Zn–Cu–

1044   Au–Ag–Te mineralization on western Milos Island, Aegean Volcanic Arc, Greece:

1045   Mineralogical, geological and geochemical constraints. Ore Geol. Rev., 53, 159–

1046   180, 2013.

1047 Anand, R. R., Paine, M., and Smith, R.E.: Genesis, Classification and Atlas of

1048   Ferruginous Materials, Yilgarn Craton. CRC LEME Open File Report vol. 13,

1049   CSIRO Exploration and Mining, Perth, 2002.

1050 Bahlburg, H. and Dobrzinski, N.: A review of the Chemical Index of Alteration (CIA)

1051   and its application to the study of Neoproterozoic glacial deposits and climate

1052   transition. Geol. Soc. London Mem., 36, 81–92, 2011.

1053 Bau, M. and Dulski, P.: Distribution of yttrium and rare- earth elements in the Penge

1054   and Kuruman Iron-Formations, oxidative scavenging of cerium on hydrous Fe

1055   oxide, Transvaal Supergroup, South Africa. Precambrian Res., 79, 37–55, 1996.

Solid Earth
Discussions

1056   Berg, I.A., Kockelkorn, D., Ramos-Vera, W.H., Say, R.F., Zarzycki, J., Hügler, M.,

1057   Alber, B.E., and Fuchs, G.: Autotrophic carbon fixation in archaea. Nat. Rev.

1058   Microbiol., 8, 447–460, 2010.

1059   Bekker, A., Slack J.F., Planavsky, N., Krapež B., Hofmann, A., Konhauser, K.O., and

1060   Rouxel, O.J.: Iron formation: The sedimentary product of a complex interplay

1061   among mantle, tectonic, oceanic, and biospheric processes. Econ. Geol., 105, 467–

1062   508, 2010.

1063   Beukes, N. J. and Klein, C.: Geochemistry and sedimentology of a facies transition—

1064   from microbanded to granular iron-formation—in the early Proterozoic Transvaal

1065   Supergroup, South Africa. Pre. Res., 47, 99–139, 1990.

1066   Blumenberg, M., Seifert, R., Reitner, J., Pape, T., and Michaelis, W.: Membrane lipid

1067   patterns typify distinct anaerobic methanotrophic consortia. Proc. Natl. Acad. Sci.

1068   U.S.A., 101, 11111–11116, 2004.

1069   Bronn, H.G.: Ubersicht der Fossilen Uberreste in den tertiären subappeninischen

1070   Gebirgen. Italiens Tertiär-Gebilde und deren organische Einschlüsse. Heidelberg

1071   pp. XII + 176 + 1 pl, 1831.

1072   Bouma, A.H.: Sedimentology of Some Flysch Deposits. Amsterdam, Elsevier, pp.

1073   168, 1962.

1074   Breitkreuz, C.: Spherulites and lithophysae—200 years of investigation on

1075   hightemperature crystallization domains in silica-rich volcanic rocks. Bull.

1076   Volcanol., 75, 1–16, 2013.

1077   Böstrom, K., Honnorez, J., Joensuu, O., and Rydell, H.: Chemistry of hydrothermal

1078   solutions in drill hole GPK-1, Palaea Kameni, Santorini, Greece. Proceedings of

1079   the third international congress, Santorini, Greece. 3, 257–260, 1990.

1080   Bühring, S.I., Elvert, M., and Witte, U.: The microbial community structure of

1081   different permeable sandy sediments characterized by the investigation of bacterial

1082   fatty acids and fluorescence in situ hybridization. Environ. Microbiol., 7, 281–293,

1083   2005.

1084   Canuel, E.A. and Marten, C.S.: Reactivity of recently deposited organic matter:

1085   Degradation of lipid compounds near the sediment-water interface. Geochim.

1086   Cosmo. Acta, 60, 1793–1806, 1996.

1087   Canet, C., Prol-Ledesma, R.M., Torres-Alvarado, I., Gilg, H.A., Villanueva, R.E., and

1088   Cruz, R.L.S.: Silica-carbonate stromatolites related to coastal hydrothennal venting

1089   in Bahia Concepcion, Baja California Sur, Mexico. Sed. Geol., 174, 97–113, 2005.

1090   Cattaneo, A. and Steel, R.J.: Transgressive deposits: a review of their variability.

1091   Earth Sci. Rev., 62, 187–228, 2003.

1092   Chi Fru, E., Ivarsson, M., Kilias, S.P., Bengtson, S., Belivanova, V., Marone, F.,

1093   Fortin, D., Broman, C., and Stampanoni, M.: Fossilized iron bacteria reveal a

1094   pathway to the origin banded iron formations. Nat. Comm., 4, 2050 DOI:

1095   10.1038/ncomms3050, 2013.

1096   Chi Fru, E., Ivarsson, M., Kilias, S.P., Frings, P.J., Hemmingsson, C., Broman, C.,

1097   Bengtson, S. and Chatzitheodoridis, E.: Biogenicity of an Early Quaternary iron

1098   formation, Milos Island, Greece. Geobiology, 13, 225–44, 2015.

1099   Dando, P.R., Hughes, J.A., Leahy, Y., Niven, S.J., Taylor, L.J. and Smith, C.: Gas

1100   venting rates from submarine hydrothermal areas around the island of Milos,

1101   Hellenic Volcanic Arc. Cont. Shelf Res., 15, 913–925, 1995.

1102   Dieke, P. Concentration of Mn and separation from Fe in sediments—I.

1103   Kinetics and stoichiometry of the reaction between birnessite and

1104   dissolved Fe(II) at 10°C. Geochim. Cosmo. Acta, 49, 1023–1033, 1985.

1105   Dorr, J.V.N.: Supergene iron ores of Minas Gerais, Brazil. Econ. Geol., 59, 1203,

1106   1964.

1107   Dowling, N.J. E., Widdel, F., and White, D.C.: Phospholipid ester-linked fatty-acid

1108   biomarkers of acetate-oxidizing sulfate-reducers and other sulfide-forming

1109   bacteria. J. Gen. Microbiol., 132, 1815–1825, 1986.

1110   Druitt, T. H. L., Edwards, R. M., Mellors, D. M., Pyle, R. S. J., Sparks, M., Lanphere,

1111   M. D., and Barreirio, B.; Santorini Volcano. Geol. Soc. Mem. London, 19, 165,

1112   1999.

1113   Fischer, W.W. and Knoll, A.H.: An iron shuttle for deepwater silica in Late Archean

1114   and early Paleoproterozoic iron formation. Geol. Soc. Am. Bull., 121, 222–235,

1115   2009.

1116   Franco, A.C., Hernández-Ayón, J.M, Beie,r E., Garçon, V., Maske, H., Paulmier, A.,

1117   Färber-Lorda, J., Castro, R., and Sosa-Ávalos, R.: Air-sea CO_2 fluxes above the

1118   stratified oxygen minimum zone in the coastal region off Mexico. J. Geophy. Res.,

1119   119, 2923–2937, 2014.

1120   Friedrich, W.L., Kromer, B., Friedrich, M., Heinemeier, J., Pfeiffer, T., and Talamo,

1121   S.: Santorini eruption radiocarbon dated to 1627-1600 BC. Science, 312, 548–548,

1122   2006.

1123   Fytikas, M., Innocenti, F., Kolios, N., Manetti, P., Mazzuoli, R., Poli, G., Rita, F., and

1124   Villari, L.: Volcanology and petrology of volcanic products from the island of

1125   Milos and neighbouring islets. J. Volcanol. Geotherm. Res., 28, 297–317, 1986.

1126   Galan, L.D.P., Doval, M., La Iglesia, A., Soriano, J., and Chavez, L.: Occurrence of

1127   silica polymorphs nanocrystals in tuffaceous rocks, Province of the Mesa Central,

1128   Mexico, and their formation from subcritical Si-rich fluids. Am. Mineral., 98, 977–

1129   985, 2013.

1130 Georgalas, G., and Liatsikas, N.: Die Historische entwickelung des Dafni-Ausbruches

1131 1925-1926. In Santorin, Der Werdegand eines Inselvulkans und sein Ausbruch

1132 1925-1928, V. 2 (ed. Reck, H.). Verlag von Dietrich Reimer, Berlin, 1–96 pp,

1133 1936.

1134 Glasby, G.P. and Schulz, H.D.: Eh, pH diagrams for Mn, Fe, Co, Ni, Cu and As under

1135 seawater conditions: application of two new types of the Eh, pH diagrams to the

1136 study of specific problems in marine geochemistry. Aquatic Geochem., 5, 227–

1137 248, 1999.

1138 Glasby, G.P., Papavassiliou, C.T., Mitsis, J., and Valsami-Jones, E.: The Vani

1139 manganese   deposit,   Milos   island,   Greece: A   fossil   stratabound

1140 Mn−Ba−Pb−Zn−As−Sb−W-rich hydrothermal deposit. Develop. Volcanol., 7,

1141 255–291, 2005.

1142 Gromet, L.P., Dymek, R.F., Haskin, L.A., and Korotev, R.L.: The North American

1143 shale composit: Its compilation and major trace element characteristics. Geochim.

1144 Cosmo. Acta, 48, 2469–2482, 1984.

1145 Gross, G.A.: A classification of iron-formation based on depositional Environments.

1146 Can. Min., 18, 215–222, 1980.

1147 Han, C., Xiao, W., Su, B., Chen, Z., Zhang, X., Ao, S., Zhang, J., Zhang ,Z., Wan, B.,

1148 Song, D., and Wang, Z.: Neoarchean Algoma-type banded iron formations from

1149 Eastern Hebei, North China Craton: SHRIMP U-Pb age, origin and tectonic

1150 setting. Precam. Res., 251, 212–231, 2014.

1151 Handley, K. M., Boothman, C., Mills, R. A., Pancost, R. D., and Lloyd, J. R.:

1152 Functional diversity of bacteria in a ferruginous hydrothermal sediment. ISME J.,

1153 4, 1193-1205, 2010.

1154 Hanert, H. H.: Bacterial and chemical iron oxide deposition in a shallow bay on

1155   Palaea Kameni, Santorini, Greece: microscopy, electron probe microanalysis, and

1156   photometry of in situ experiments. Geomicrobiol. J., 19, 317–342, 2002.

1157 Hein, J. R. and Conrad, T. A.: Copper-nickel-rich, amalgamated ferromanganese

1158   crust-nodule deposits froms Shatsky Rise, NW Pacific. Geochem. Geophy.

1159   Geosyst., 13, Q10022, doi:10.1029/2012GC004286, 2012.

1160 Hein, J. R., Stamatakis, M. G., and Dowling, J. S.: Trace metal-rich Quaternary

1161   hydrothermal manganese oxide and barite deposit, Milos Island, Greece. Applied

1162   Earth Science: Trans. Inst. Min. Metal. Section B., 109, 67–76, 2000.

1163 Hickman, A.H.: Regional review of the 34236–3350 Ma Strelley Pool Formation,

1164   Pilbara Craton, Western Australia. Geol Survey West Australia, 215, 1-23, 2008.

1165 Horwell, C.J., le Blond, S., Michnowicz, S. A. K. and Cressey, G.: Cristobalite in a

1166   rhyolitic lava dome: evolution of ash hazard. Bull. Volcanol. 72, 249-253, 2010.

1167 Ichihara, K. and Fukubayashi, Y.: Preparation of fatty acid methyl esters for gas-

1168   liquid chromatography. J. Lipid Res., 51, 635–40, 2010.

1169 James, H. L.: Sedimentary facies of iron-formation. Econ. Geol., 49, 235−293, 1954.

1170 James, H. L.: Distribution of banded iron-formation in space and time. Dev. Pre.

1171   Geol., 6, 471–490, 1983.

1172 Johnson, C. M., Beard, B. L., and Roden, E. E.: The iron isotope fingerprints of redox

1173   and biogeochemical cycling in modern and ancient Earth. Ann. Rev. Earth Plan.

1174   Sci., 36, 457–493, 2008.

1175 Kappler, A., Pasquero, C., and Newman, D.K.: Deposition of banded iron formations

1176   by anoxygenic phototrophic Fe(II)-oxidizing bacteria. Geology, 33, 865–868,

1177   2005.

Solid Earth
Discussions

Open Access

EGU

1178 Kilias, S. P., Detsi, K., Godelitsas, A., Typas, M., Naden, J., and Marantos, Y.:

1179 Evidence of Mn-oxide biomineralization, Vani Mn deposit, Milos, Greece. In:

1180 Proceedings of the ninth biennial Meeting of the Society for Geology Applied to

1181 Mineral Deposits, Dublin, Ireland. Irish Assoc. Econ. Geol. 1069–1072 pp, 2007.

1182 Kilias, S. P.: Microbial mat-related structures in the Quaternary Cape Vani

1183 manganese-oxide (-barite) deposit, NW Milos island, Greece. Soc. Sed. Geol. Sp.

1184 Pub., 101, 97–110, 2011.

1185 Kilias, S. P., Chatzitheodoridis, E., and Lyon, I.: Molecular, chemical and

1186 morphological evidence for hematite biogenicity at the Quaternary Cape Vani Mn-

1187 (Ba-Fe) deposit, Milos, Greece. Bull. Geol. Soc., 47, 834-842, 2013.

1188 Konhauser, K. O., Planavsky, N. J., Hardisty, D. S., Robbins, L. J., Warchola, T. J.,

1189 Haugaard, R., Lalonde, S. V., Partin, C. A., Oonk, P .B. H., Tsikos, H., and Lyons,

1190 T.W.: Iron formations: A global record of Neoarchaean to Palaeoproterozoic

1191 environmental history. Earth Sci. Rev., doi: 10.1016/j.earscirev.2017.06.012, 2017.

1192 Kilias, P. S., Nomikou, P., Papanikolaou, D., Polymenakou, P. N., Godelitsas, A.,

1193 Argyraki, A., Carey, S., Gamaletsos, P., Mertzimekis, T. J., Stathopoulou, E.,

1194 Goettlicher, J., Steininger, R., Betzelou, K., Livanos, I., Christakis, C., Bell, K. C.:

1195 and Scoullos, M. New insights into hydrothermal vent processes in the unique

1196 shallow-submarine arc-volcano, Kolumbo (Santorini), Greece. Sci. Rep., 3,

1197 doi:10.1038/srep02421, 2013.

1198 Klein, C.: Some Precambrian banded iron-formations (BIFs) from around the world:

1199 Their age, geologic setting, mineralogy, metamorphism, geochemistry, and origins.

1200 Am. Min., 90, 1473–1499, 2005.

1201 Kling, G. W., Evans, W. C., Tanyileke, G., Kusakabe, M., Ohba, T., Yoshida, Y., and

1202   Hell, J. V.: Degassing Lakes Nyos and Monoun: Defusing certain disaster. Proc.

1203   Natl. Acad. Sci. U.S.A., 102, 14185–14190, 2005.

1204 Konhauser, K. O., Hamade, T., Riaswell., R., Morris, R. C., Ferris, F. G., Southam, G.

1205   and Canfied, D. E.: Could bacteria have formed the Precambrian banded iron

1206   formations? Geology, 12, 1097–1082, 2002.

1207 Krapež, B., Barley, M. E., Pickard, A .L.: Hydrothermal and resedimented origins of

1208   the precursor sediments to banded iron formations: Sedimentological evidence

1209   from the early Palaeoproterozoic Brockman Supersequence of Western Australia.

1210   Sedimentology, 50, 979-1011, 2003.

1211 Lalonde, K., Mucci, A., Quellet, A. and Gélinas, Y.: Preservation of organic matter in

1212   sediments promoted by iron. Nature, 483, 198–200, 2012.

1213 Levett, A., Gagen, E., Shuster, J., Rintoul, L., Tobin, M., Vongsvivut, J., Bambery,

1214   K., Vasconcelos, P., and Southam, G.: Evidence of biogeochemical processes in

1215   iron duricrust formation. J. South. Am. Earth Sci., 71, 131–142, 2016.

1216 Li, W., Czaja, A. D., Van Kranendonk, M. J., Beard, B. L., Roden, E. E., Johnson, C.

1217   M.: An anoxic, Fe(II)-rich, U-poor ocean 3.46 billion years ago. Geochim. Cosmo.

1218   Acta, 120, 65-79, 2013.

1219 Liakopoulos, A., Glasby, G. P., Papavassiliou, C. T. and Boulegue, J.: Nature and

1220   origin of the Vani manganese deposit, Milos, Greece: an overview. Ore Geol. Rev.,

1221   18, 181–209, 2001.

1222 Lowe, D.R.: Sediment gravity flows: II. Depositional models with special reference to

1223   the deposits of high-density turbidity currents. J. Sed. Petrol., 52, 279–297, 1982.

1224 Lowe, D.R.: Restricted shallow-water sedimentation of earlyArchaean stromatolitic

1225   and evaporitic strata of the Strelley Pool Chert, Pilbara Block, Western Australia.

1226   Precam. Res., 19, 239–283, 1983.

1227 Lowe, D.R.: Shallow-water sedimentation of accretionary lapilli-bearing strata of the

1228   Msauli Chert: Evidence of explosive hydromagmatic komatiitic volcanism. In:

1229   Geologic Evolution of the Barberton Greenstone Belt, South Africa. Geol. Soc.

1230   Am., Boulder, Colorado, 213-232 pp, 1999.

1231 Lü, D., Song, Q., and Wang, X.: Decomposition of algal lipids in clay-enriched

1232   marine sediment under oxic and anoxic conditions. Chin. J. Oceanogr. Limnol., 28,

1233   131–143, 2010.

1234 Marschik, R., Bauer, T., Hensler, A.-S., Skarpelis, N., and Hölzl, S. Isotope

1235   Geochemistry of the Pb-Zn-Ba(-Ag-Au) Mineralization at Triades-Galana, Milos

1236   Island, Greece. Res. Geol., 60, 335–347, 2010.

1237 Maynard, J. B.: Chemistry of modern soils as a guide to interpreting Precambrian

1238   Paleosols. J. Geol., 100, 279–289, 1993.

1239 Maynard, J. B.: The chemistry of manganese ores through time: a signal of increasing

1240   diversity of earth-surface environments. Econ. Geol., 105, 535–552.

1241 Miall, A. D. (1978) Lithofacies types and vertical profile models in braided river

1242   deposits. Can. Soc. Pet. Geol. Mem., 5, 597–604, 2010.

1243 Miall, A. D.: Architectural element analysis: a new method of facies analysis applied

1244   to fluvial deposits. Earth Sci. Rev., 22, 261e308, 1985.

1245 Morris, R. V., Vaniman, D. T., Blake, D. F., Gellert, R., Chipera, S. J., Rampe, E. B.,

1246   Ming, D. W., Morrison, S. M., Downs, R. T., Treiman, A. H., Yen, A. S.,

1247   Grotzinger, J. P., Achilles, C. N., Bristow, T. F., Crisp, J. A., Des Marais, D. J.,

1248   Farmer, J. D., Fendrich, K. V., Frydenvang, J., Gradd, T. G., Morookian, J-M.,

1249   Stolper, E. M. and Schwenzer, S. P.: Silicic volcanism on Mars evidenced by

1250   tridymite in high-SiO2 sedimentary rock at Gale crater. Proc. Natl. Acad. Sci.

1251   U.S.A., 113, 7071–7076, 2016.

1252   Mutti, E.: Turbidite Sandstones. Agip Spe. Pub., 275 pp, 1992.

1253   Nesbitt, H. W. and Young, G. M.: Early Proterozoic climates and plate motions

1254   inferred from major element chemistry of lutites. Nature, 199, 715–717, 1982.

1255   Nijman, W., De Bruin, K., and Valkering, M.: Growth fault control of early Archean

1256   cherts, barite mounds, and chert-barite veins, North Pole Dome, Eastern Pilbara,

1257   Western Australia. Precam. Res., 88, 25–52, 1998.

1258   Noffke, N., Hazen, R., and Nhleko, N.: Earth's earliest microbial mats in a

1259   siliciclastic marine environment (2.9 Ga Mozaan Group, South Africa). Geology,

1260   31, 673–676, 2003.

1261   Nomikou, P., Papanikolaou, D., Alexandri, M., Sakellariou, D., and Rousakis, G.:

1262   Submarine volcanoes along the Aegean volcanic arc. Tectonophysics, 597–598,

1263   123–146, 2013.

1264   Nomikou, P., Parks, M. M., Papanikolaou, D., Pyle, D. M., Mather, T. A., Carey, S.,

1265   Watts, A. B., Paulatto, M., Kalnins, M.L., Livanos, I., and Bejelou, K.: The

1266   emergence and growth of a submarine volcano: The Kameni islands, Santorini

1267   (Greece). Geo. Res. J., 1, 8–18, 2014.

1268   Orme, D. A. and Laskowski, A. K.: Basin Analysis of the Albian–Santonian Xigaze

1269   Forearc, Lazi Region, South-Central Tibet. J. Sed. Res., 86, 894-913, 2016.

1270   Ossa, F. O., Hofmann, A., Vidal, O., Kramers, J. D., Belyanin, G. and Cavalazzi, B.:

1271   Unusual manganese enrichment in the Mesoarchean Mozaan Group, Pongola

1272   Supergroup, South Africa. Pre. Res., 281, 414-433, 2016.

1273   Ozawa, A., Ueda, A., Fantong, W. Y., Anazawa, K., Yoshida, Y., Kusakabe, M.,

1274   Ohba, T., Tanyileke, G., and Hell, J.V. Rate of siderite precipitation in Lake Nyos,

1275   Cameroon. Geol. Soc. London Sp. Pub., 437, doi.org/10.1144/SP437.13, 2016.

1276   Papanikolaou, D., Lekkas, E., and Syskakis, D.: Tectonic analysis of the geothermal

1277   field of Milos Island. Bull. Geol. Soc. Greece, 24, 27–46, 1990.

1278   Papavassiliou, K., Voudouris, P., Kanellopoulos, C., Glasby, G., Alfieris, D., and

1279   Mitsis, I.: New geochemical and mineralogical constraints on the genesis of the

1280   Vani hydrothermal manganese deposit at NW Milos island, Greece: Comparison

1281   with the Aspro Gialoudi deposit and implications for the formation of the Milos

1282   manganese mineralization. Ore Geol., 80, 594–611, 2017.

1283   Papike, J. J., Karner, J. M., Shearer, C. K. and Burger, P. V.: Silicate mineralogy of

1284   martian meteorites. Geochim. Cosmochim. Acta, 73, 7443–7485, 2009.

1285   Paulmier, A., Ruíz-Pino, D., and Garçon, V.: The oxygen minimum zone (OMZ) off

1286   Chile as intense source of CO2 and N2O, Cont. Shelf. Res., 28, 2746–2756, 2008.

1287   Percoits, E., Gingras, M. K., Barley, M. E., Kapper, A., Posth, N. R., and Konhauser,

1288   K.O.: Petrography and geochemistry of the Dales Gorge banded iron formation:

1289   Paragenetic sequence, source and implications for palaeo-ocean chemistry. Pre.

1290   Res., 172, 2009.

1291   Paulmier, A., Ruiz-Pino, D., and Gaçon, V.: CO_2 maximum in the oxygen minimum

1292   zone (OMZ). Biogeosciences, 8, 239–252. doi:10.5194/bg-8-239-2011, 2011.

1293   Pichler, T. and Dix, G. R. Hydrothermal venting within a coral reef ecosystem,

1294   Ambitle Island, Papua New Guinea. Geology, 50, 435–438, 1996.

1295   Pichler, T. and Veizer, J.: Precipitation of Fe(III) oxyhydroxide deposits from

1296   shallow-water hydrothermal fluids in Tutum Bay, Ambitle Island, Papua New

1297   Guinea. Chem. Geol., 162, 15–31, 1999.

1298   Pichler, T. and Veizer, J. The precipitation of aragonite from shallow-water

1299   hydrothermal fluids in a coral reef, Tutum Bay, Ambitle Island, Papua New

1300   Guinea. Chem. Geol., 207, 317–45, 2004.

1301   Planavsky, N., Rouxel, O., Bekker, A., Shapiro, R., Fralick, P., and Knudsen, A.:

1302   Iron-oxidizing microbial ecosystems thrived in late Paleoproterozoic redox-

1303   stratified oceans. Earth Plan. Sci. Letts., 286, 2307–242, 2009.

1304   Planavsky, N. J., Bekker, A., Rouxel, O. J., Kamber, B., Hofmann, A., Knudsen, A.

1305   and Lyons T. W.: Rare Earth element and yttrium compositions of Archean and

1306   Paleoproterozoic Fe formations revisited: New perspectives on the significance

1307   and mechanisms of deposition. Geochim. Cosmo. Acta, 74, 6387–6405, 2010.

1308   Plimer, I. Milos Geologic History. Koan Publishing House, Athens, Greece. 261 pp,

1309   2000.

1310   Poulton, S.W. and Canfield, D.E.: Ferruginous conditions: A dominant feature of the

1311   ocean through Earth's history. Elements. 7, 107-112, 2011.

1312   Preuß, A., Schauder, R., Fuchs, G., and Stichler W.: Carbon isotope fractionation by

1313   autototrophic bacteria with three different CO_2 fixation pathways. Zeitschrift für

1314   Naturforschung C., 44, 397–402, 1989.

1315   Pufahl, P. K. and Fralick, P. W.: Depositional controls on Palaeoproterozoic iron

1316   formation accumulation, Gogebic range, Lake Superior region, USA.

1317   Sedimentology, 51, 791–808, 2004.

1318   Pufahl, P. K., Anderson, S. L., and Hiatt, E. E.: Dynamic sedimentation of

1319   Paleoproterozoic continental margin iron formation, Labrador Trough, Canada:

1320   Paleoenvironments and sequence stratigraphy. Sed. Geol., 309, 48–65, 2014.

1321   Ramos, E., Marzo, M., de Gibert, J. M., Tawengi, K. S., Khoja, A. A., and Bolatti, N.

1322   D.: Stratigraphy and sedimentology of the middle Ordovician Hawaz formation

1323   (Murzuq Basin, Libya). AAPG bull., 90, 1309-1336, 2006.

1324   Rancourt, D. G., Fortin, D., Pichler, T., and Lamarche, G.: Mineralogical

1325   characterization of a natural very As-rich hydrous ferric oxide coprecipitate formed

1326   by mixing of hydrothermal fluid and sea water. Am. Min., 86, 834–851, 2001.

1327   Rasmussen, B., Meier, D. B., Krapež. B., and Muhling, J. R.: Iron silicate

1328   microgranules as precursor sediments to 2.5-billion-year-old banded iron

1329   formations. Geology, 41, 435–438, 2013.

1330   Rasmussen, B., Krapež, B., and Meier, D. B. Replacement origin for hematite in 2.5

1331   Ga banded iron formation: Evidence for postdepositional oxidation of iron-bearing

1332   minerals. Geol. Soc. Am. Bull., 126, 438–446, 2014.

1333   Riedel, T., Zak, D., Biester, H., and Dittmar, T.: Iron traps terrestrially derived

1334   dissolved organic matter at redox interfaces. Proc. Nat. Acad. Sci. U.S.A., 110,

1335   10101–10105, 2013.

1336   Robbins, E. I., Kourtidou-Papadeli, C., Iberall, A. S., Nord, Jr, G. L. and Sato, M.:

1337   From Precambrian Iron-Formation to Terraforming Mars: The JIMES Expedition

1338   to Santorini. Geomicrobiol. J., 33, 630–645, 2016.

1339   Roy, S.: Manganese Mineralization: Geochemistry and mineralogy of terrestrial and

1340   marine deposits. Geol. Soc. Spe. Pub., 119, 5–27, 1997.

1341   Roy, S.: Sedimentary manganese metallogenesis in response to the evolution of the

1342   Earth system. Earth-Sci. Rev., 77, 273–305, 2006.

1343   Rudnick, R. and Gao, S. Composition of the continental crust. In: Treatise on

1344   Geochemistry, vol. 3. Elsevier–Pergamon, Oxford, 1–64 pp, 2003.

Solid Earth
Discussions

Open Access

EGU

1345   Shanmugam, G.: Submarine fans: a critical retrospective (1950–2015). J.

1346   Palaeogeogr., 5, 110-184, 2016.

1347   Schwertmann, U. and Murad, E. Effect of pH on the formation of goethite and

1348   hematite from ferrihydrite. Clay Clay Min., 31, 277–284, 1983.

1349   Shuster, D. L., Farley, K. A., Vasconcelos, P. M., Balco, G., Monteiro, H. S.,

1350   Waltenberg, K., and Stone, J. O. Cosmogenic 3 He in hematite and goethite from

1351   Brazilian "canga" duricrust demonstrates the extreme stability of these surfaces.

1352   Earth Plan. Sci. Lett., 329, 41–50, 2012.

1353   Sigurdsson, H., Carey, S., Alexandri, M., Vougioukalakis, G., Croff, K., Roman, C.,

1354   Sakellariou, D., Anagnostou, C., Rousakis, G., Loakim, C., Goguo, A., Ballas, D.,

1355   Misaridis, T., and Nomikou, P. Marine investigations of Greece's Santorini

1356   volcanic field. EOS Trans. Am. Geophy. Union, 87, 337–342, 2003.

1357   Simonson, B. M.: Sedimentological constraints on the origins of Precambrian iron-

1358   formations. Geol. Soc. Am. Bull., 96, 244–252, 1985.

1359   Simonson, B. M.: Origin and evolution of large Precambrian iron formations. Geol.

1360   Soc. Am., 370, 231−244, 2003.

1361   Simonson, B. M. and Goode, A. D. T.: First discivery of ferruginous chert arenites in

1362   the early Precambrian Hamersley Group of Western Australia. Geology, 17, 269–

1363   272, 1989.

1364   Simonson, B. M. and Hassler, S. W.: Was the deposition of large Precambrian iron

1365   formations linked to major marine transgressions? The J. Geol., 104, 665−676,

1366   1996.

1367   Skarpelis, N. and Koutles, T.: Geology of epithermal mineralization of the NW part of

1368   Milos Island, Greece. In Proceedings of the 5th International Symposium on

1369   Eastern Mediterranean Geology. (eds. Chatzipetros, A. & Pavlides S). School of

1370   Geology, Aristotelian University of Thessaloniki, Thessaloniki, Greece. pp. 1449–

1371   1452, 2004.

1372   Steel, R.J., Rasmussen, H., Eide, S., Neuman, B., and Siggerud, E. I. H. Anatomy of

1373   high-sediment-supply, transgressive tracts in the Vilomara composite sequence,

1374   Sant Llorenc del Munt, Ebro basin, NE Spain. Sed. Geol., 138, 125–142, 2000.

1375   Stewart, A. L. and Mcphie, J.: Facies architecture and Late Ploicene – Pleistocene

1376   evolution of a felsic volcanic island, Milo, Greece. Bull. Volcanol. 68, 703–726,

1377   2006.

1378   Sun, S., Konhauser, K. O., Kappler, A., and Li, Y.-L.: Primary hematite in

1379   Neoarchean to Paleoproterozoic oceans. GSA Bull., 127, 850–861, 2015.

1380   Stüben, D. and Glasby, G.P.: Geochemistry of shallow submarine hydrothermal fluids

1381   from Paleohori Bay, Milos, Aegean Sea. Exp. Min. Geol., 8, 273–287, 1999.

1382   Swamy, V., Saxena, S. K., Sundman, B., and Zhang, J. A thermodynamic assessment

1383   of silica phase diagram. J. Geophys. Res. Solid Earth, 99, 11787–11794, 1994.

1384   Taylor, J., and Parkes, R. J.: The cellular fatty-acids of the sulfate-reducing bacteria,

1385   Desulfobacter sp., Desulfobulbus sp. and Desulfovibrio desulfuricans. J. Gen.

1386   Microbiol., 129, 3303–3309, 1983.

1387   Tice, M. M. and Lowe, D. R.: The origin of carbonaceous matter in pre-3.0 Ga

1388   greenstone terrains: A review and new evidence from the 3.42 Ga Buck Reef

1389   Chert. Earth Sci. Rev., 76, 259–300, 2006.

1390   Stiegler, M. T., Lowe, D. R., and Byerly, G. R.: Abundant pyroclastic komatiitic

1391   volcanism in the 3.5-3.2 Ga Barberton greenstone belt, South Africa. Geology, 36,

1392   779–782, 2008.

1393   Tiodjio, R. M., Sakatoku, A., Nakamura, A., Tanaka, A., Fantong, W. Y., Tchakam,

1394   K. B., Tanyileke, G., Ohba, T., Hell, V. J., Kusakabe, M., Nakamura, S., and Ueda,

1395   A.: Bacterial and archaeal communities in Lake Nyos (Cameroon, Central Africa).

1396   Sci. Rep., 4, 6151, DOI: 10.1038/srep06151, 2014.

1397   Trendall, A.F.: The significance of iron-formation in the Precambrian stratigraphic

1398   record. Int. Assoc. Sed. Spe. Pub., 33, 33–66, 2002.

1399   Trower, E. J. and Lowe, D. R.: Sedimentology of the ~3.3 Ga upper Mendon

1400   Formation, Barberton Greenstone Belt, South Africa. Pre. Res., 281, 473–494,

1401   2016.

1402   Tsikos, H., Mathews, A., Erel, Y., and Moore, J.M.: Iron isotopes constrain

1403   biogeochemical redox cycling of iron and manganese in a Palaeoproterozoic

1404   stratified basin. Earth Planet. Sci. Lett., 298, 125–134, 2010.

1405   van Hinsbergen, D. J. J., Snel, E., Garstman, S. A., Mărunţeanu, M., Langereis, C. G.,

1406   Wortel, M. J. R., and Meulenkamp, J. E.: Vertical motions in the Aegean volcanic

1407   arc: evidence for rapid subsidence preceding volcanic activity on Milos and

1408   Aegina. Mar. Geol., 209, 329–345, 2004.

1409   Varnavas, S. P. and Cronan, D. S.: Submarine hydrothermal activity off Santorini and

1410   Milos in the Central Hellenic Volcanic Arc: A synthesis. Chem. Geol., 224, 40–54,

1411   2005.

1412   Weber, K. A., Achenbach, L. A., and Coates, J. D.: Microorganisms pumping iron:

1413   anaerobic microbial iron oxidation and reduction. Nat. Rev. Microbiol., 4, 752–64,

1414   2006.

1415

1416

1417

1418

1419

Solid Earth
Discussions

1420   Table 1. Table 1. Results of X-Ray Radiation (XRD) analysis showing major

1421   mineralogical compositions. NFIF (non-fossiliferous iron formation) and MFIF

1422   (microfossiliferous iron formation), respectively.

1423

Mineral phase	MFIF1	MFIF2	MFIF3	Fe-rich NFIF2A	Si-rich NFIIF2B	Fe-rich NFIF2C	Si-rich NFIFD	Fe-rich NFIF2E	Fe-rich NFIF2F
Hematite	+	+	-	+	+	+	+	+	+
Quartz	+	+	+	-	-	-	-	-	-
Sanidine	-	-	-	+	+	+	+	+	+
Tridymite	-	-	-	-	+	+	+	+	+
Cristobalite	-	-	-	+	-	-	-	-	-
Cryptomelane	-	-	+	-	-	-	-	-	-

1424
1425
1426
1427
1428
1429
1430
1431
1432
1433
1434
1435
1436
1437
1438
1439
1440
1441
1442
1443
1444
1445
1446
1447
1448
1449
1450
1451
1452
1453
1454
1455
1456
1457

1458

1459   Table 2. Stable isotope results. Letters A-F on the NFIF samples represent respective

1460   bands of the sawn rock in Figure 7E.

Sample	$\delta^{13}C_{org}$ vs PDB (‰)	C_{org} (%)	$\delta^{15}N$ vs air (‰)	N (%)	$\delta^{34}S$ vs CDT (‰)	S (%)
Fe-rich NFIF2A	-25,63	0,061	nd	0,023	nd	0,01
Si-rich NFIF2B	-25,03	0,109	nd	0,017	nd	0,02
Fe-rich NFIF2C	-24,45	0,068	nd	0,013	nd	0,02
Si-rich NFIF2D	-25,04	0,076	nd	0,015	nd	0,02
Fe-rich NFIF2E	-25,19	0,042	nd	0,009	nd	0,01
Si-rich NFIF2F	-25,49	0,050	nd	0,012	nd	0,03
MFIF1	-25,49	0,087	nd	0,017	nd	0,01
MFIF2	-26,25	0,046	nd	0,005	nd	nd
MFIF3	-25,69	0,041	nd	0,006	nd	nd

ND, Not detected

1461
1462
1463
1464
1465
1466
1467
1468

1469

1470

1471

1472

1473

1474

1475

1476

1477

1478

1479
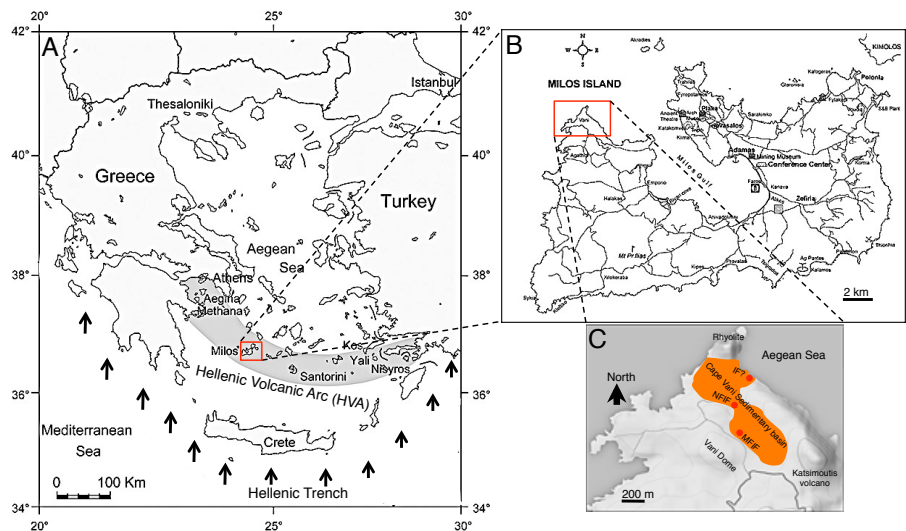
1480

1481   Fig. 1. Geological map of Milos (redrawn from Marschik et al., 2010). (A),
1482   Geotectonic map showing the position of Milos Island, along the Hellenic Volcanic
1483   Arc (HVA). Arrows indicate the direction of subduction of the African plate
1484   underneath the Euroasian plate. (B) Milos Island. (C), The Milos iron formation is
1485   located in the 8-shaped Cape Vani sedimentary basin (CVSB). At least two IFs are
1486   present in the CVSB. These are made up of a non-fossiliferous IF (NFIF) at the
1487   juncture between the two large sedimentary basins and a microfossiliferous iron
1488   formation (MFIF) located at the SW margin in the second basin. A potential third IF
1489   (IF?) is located NE, close to the present day Aegean Sea. It is however not certain if
1490   this deposit is part of the NFIF or not, because of the open mining pit separating the
1491   two.

1492

1493

Solid Earth
Discussions

Open Access

EGU
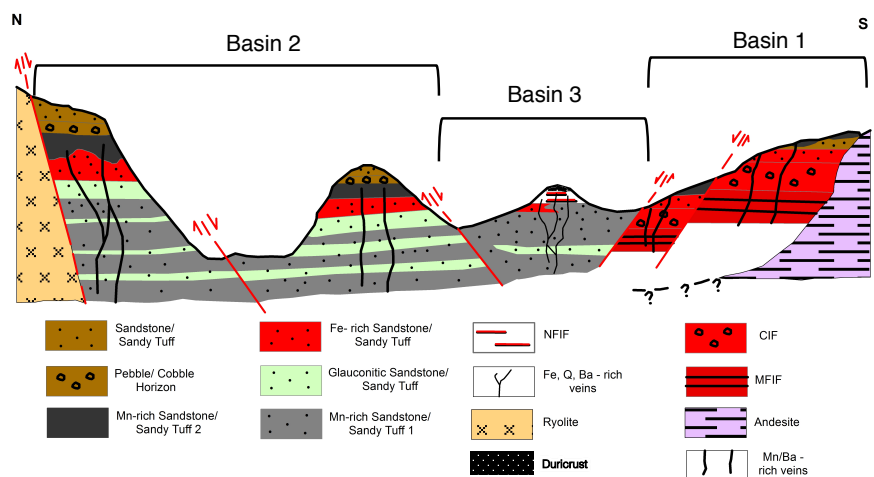
1494

Fig. 2. Generalized schematic north-south geologic cross section through the ~1 km long CVSB showing interpreted geology, relationships between the main lithofacies, main fault locations, the iron and manganese formations, in support of a proposed three-basin hypothesis. Not drawn to scale. Four types of iron-rich sedimentary rocks occur in the CVSB. These include the iron-rich sandstones, the iron-Mn-rich sandstones, the conglomerate hosted iron formation (CIF) and the MFIF and NFIF formations that are depositionally and chemically distinct from the sandstone deposits.

1503

1504
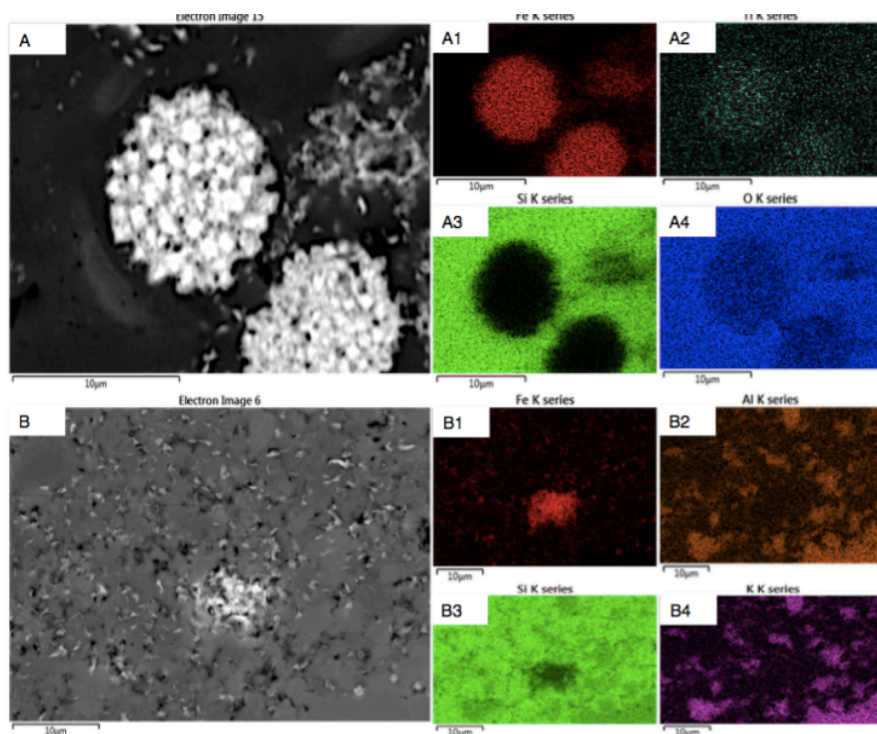
1505

Fig. 3. EDS-electron image showing different Fe-rich mineral phases in a Si-rich matrix from the MFIF. The bright colours correspond to the analysed elements. (A), framboidal hematite particles. A1-A4, different element compositions associated with framboidal particles in panel A. (B), Dispersed fluffy Fe-rich mineral grains. B1-B4, corresponding elements associated with the micrograph in panel A.

1511

1512
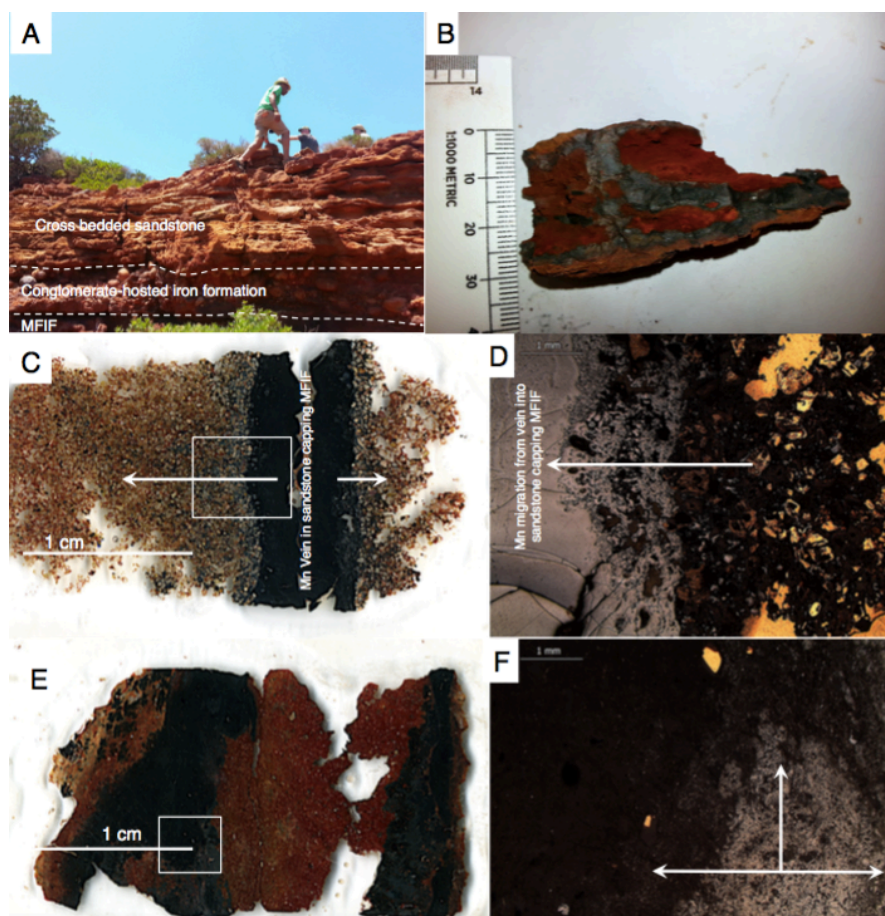
1513

Fig. 4. Sedimentary profile, thin section scans and optical microscope images of the MFIF. (A), Field photo showing the sedimentary profile of the MFIF chacterized by the overlying sandstone cap. (B), Photograph showing black diffused Mn-rich bands near the base of the MFIF. (C), Scanned image of thin section showing a black Mn-rich vein in the overlying MFIF sandstone showing a gradient of Mn migrating into the sandstone matrix (white arrows). (D), Light microscopy images showing details in panel C. (E), Scanned image of an MFIF thin section showing black Mn bands migration into a red iron-rich background. (F), Amplified light microscope image showing gray Mn layers migrating into a black Fe-rich matrix. White arrows show direction of movement. Boxes in C and E are amplified in D and F.

1526
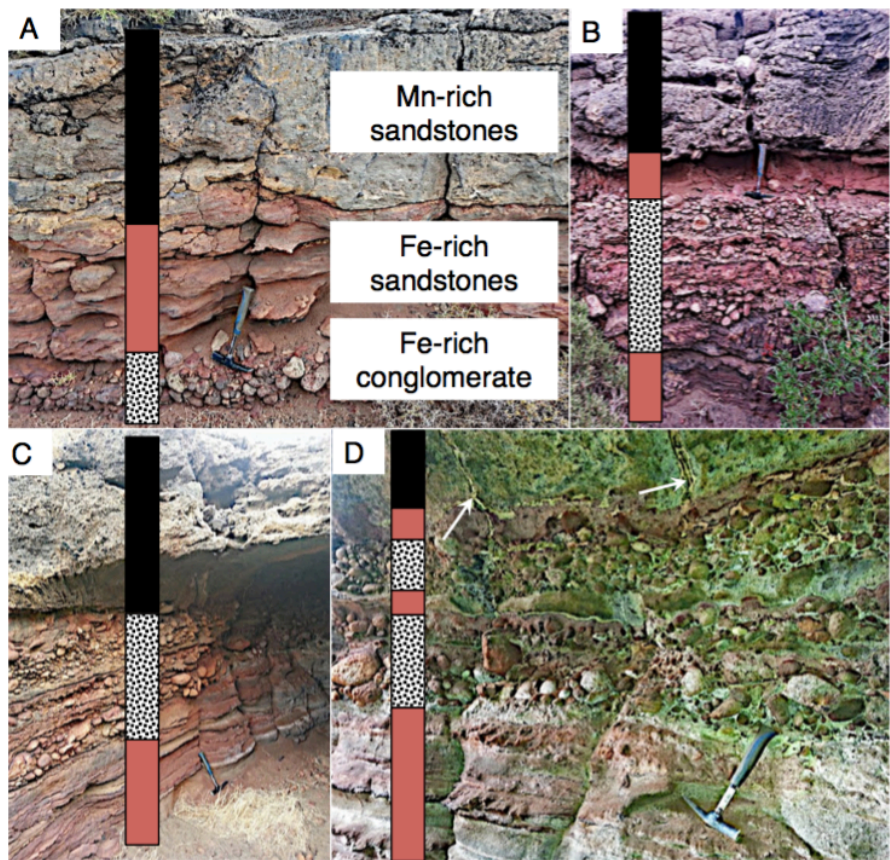
Fig. 5. Sedimentary sequence overlying the MFIF, consisting of thin (< 0.5 m)
polymictic andesite-dacite cobble-pebble, and sandstone-sandy tuff pebble, and Fe-
rich conglomerate facies overlain by thinly laminated Fe-rich sandstone beds. This
vertical sequence is interpreted to represent a progressively deeper water environment
deepening-upward sequence (A) as a result of sea level rise due to tectonic
subsidence. The multiple cycles shown in panels B-D signify several potential
episodes or sea level rise. Arrows in panel D showing hydrothermal feeder veins
feeding the overlying layers. The sequence is overlain by a thin package of parallel
and cross-bedded Mn-sandstone cap.

1536

1537
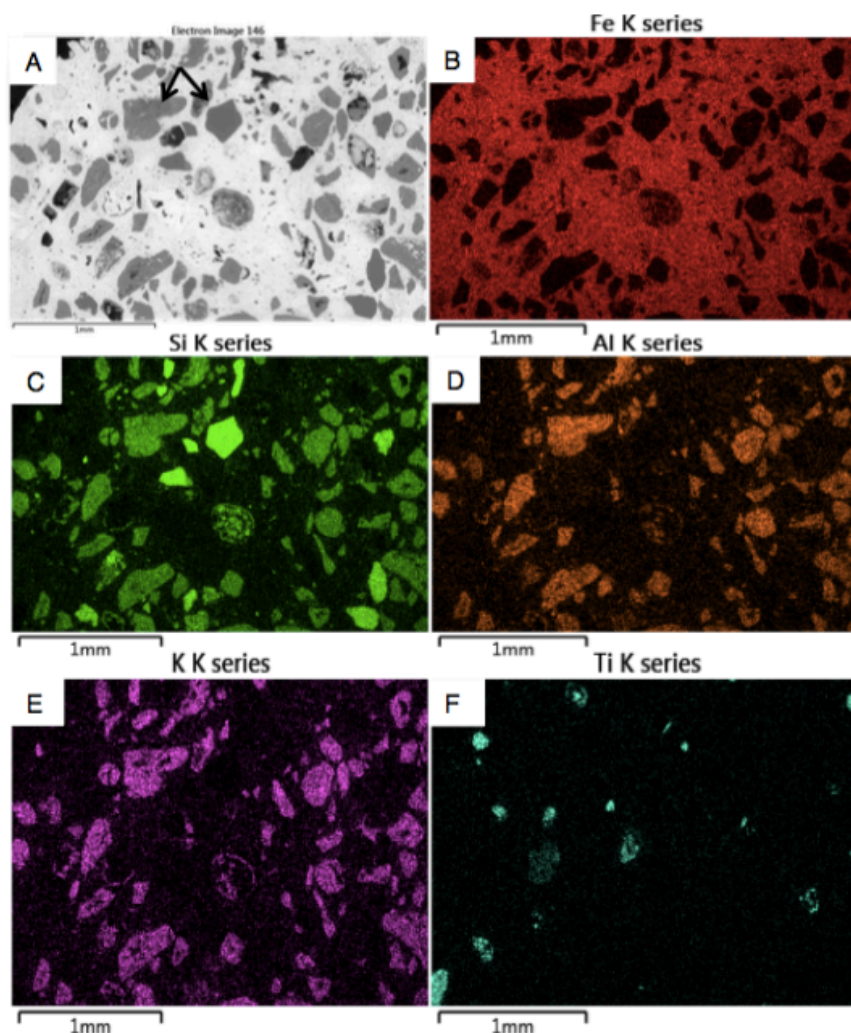
Fig. 6. Scanning electron microscope electron image of the volcaniclastic (K-feldspar)/ iron-rich sandstone layer overlying the MFIF.

Solid Earth

Discussions

Open Access

EGU
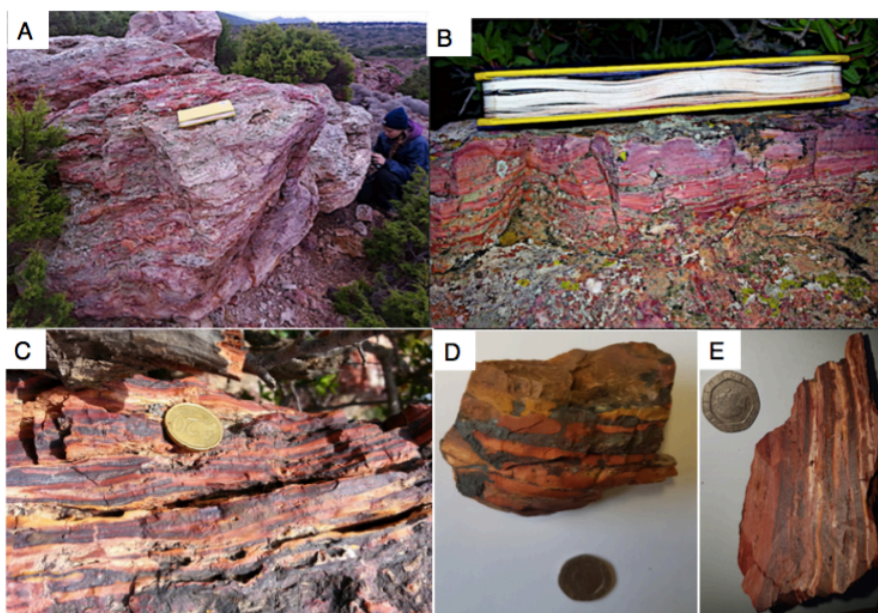
1543

Fig. 7. Typical NFIF banded iron rocks. (A-C), Field photographs. (D), Handheld banded Fe sample. (E), Sawn NFIF sample with laminated Fe-rich bands alternating with Si-rich bands.

1547

1548
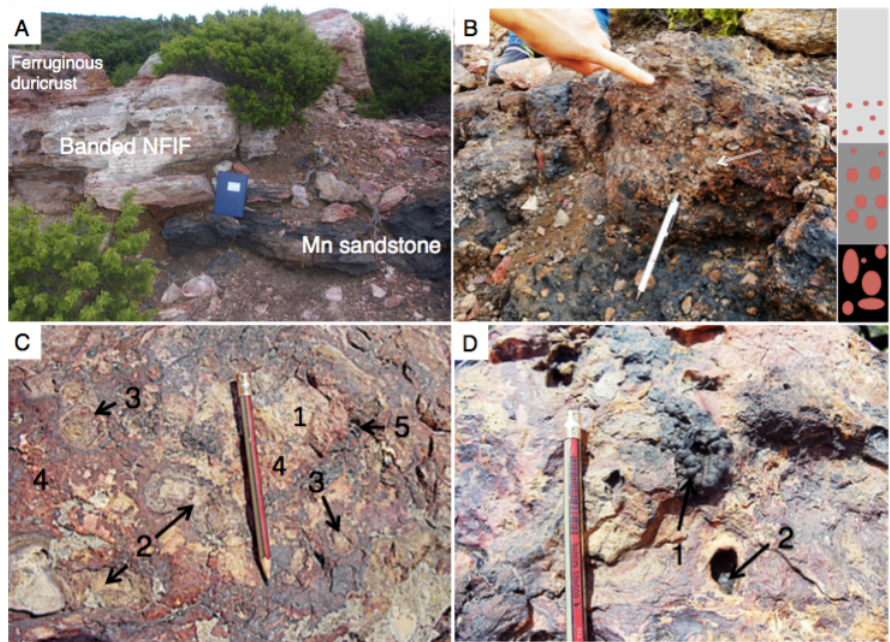
1549

Fig. 8. Field sedimentology and stratigraphy of Section B sequence containing the NFIF. (A), Sharp boundary between lower Mn sandstone and unconformably overlying NFIF capped by a ferruginous duricrust. (B), Sandstone-sandy tuff pebble to gravel conglomerate lag facies, showing an upward fining character and bored clasts (black), locally overlies the Mn sandstone and capped by a sharp erosional contact with the overlying NFIF. The tip of the pen (7 cm long) rests on late blue-black Mn oxide overprint. (C), Ferruginous duricrust that comprises lithic fragments composed of (1) Fe-nodules (2) and Fe-concretions (3) in a hematite-rich matrix (4). (D), Matrix dissolution resulting in vermiform Mn nodules (1) and cavity black Mn oxide (2) infillings, post-dating the ferruginous duricrust formation.

1562
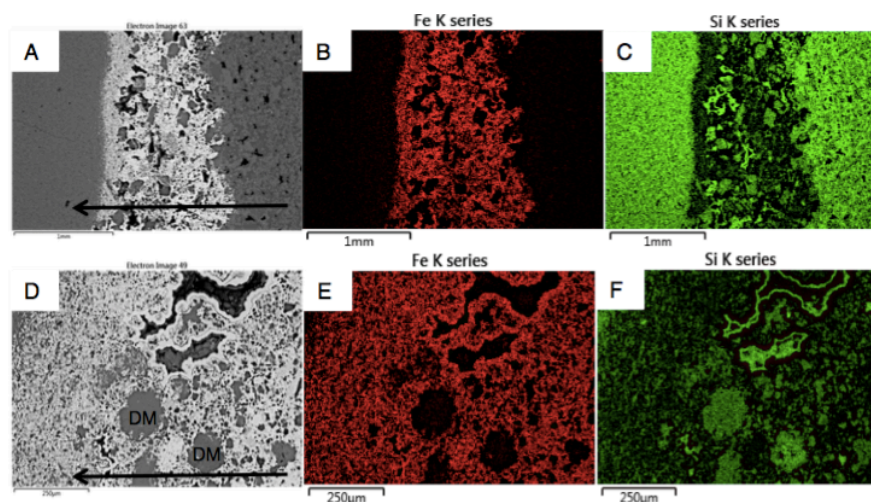
Fig. 9. EDS-electron image showing major elemental composition of typical Fe bands alternating with Si-rich layers in the NFIF. Volcaniclastic detritus mostly present in the Fe-rich bands, suggests precipitation during active submarine volcanism. To the contrary, the Si-rich bands are composed of more fine-grain, signifying deposition during periods of minimal volcanic activity. Arrows in panels (A) and (B) depict the direction of sedimentation, which was often seen to proceed from an Fe-rich matrix mixed with large grains of volcaniclastic detritus (DM) to one composed essentially of very fine-grained Fe particles before transitioning into the very fine-grained Si-rich layer. An upward fining of the volcaniclastic particles in the Fe-rich layers transitions from one made up of volcaniclastic debris and hematite, to a mainly thin hematite-rich horizon at the top of this mixed layer (see supplementary Figs 8-11 for details). This concurrent occurrence of volcaniclast and Fe oxides and the upward fining nature of the Fe-rich layers, suggest the release and oxidation of Fe(II) coincided with the settling of hydrothermal debris resulting from the introduction of enormous amount of reduced materials into the water column (Bekker et al., 2010). The iron-rich layer ceased forming as hydrothermal/volcanic release of Fe subsided, followed by deposition of the Si-rich layer. This repetitive cycle of events is observed for tens of metres laterally and vertically, stressing that the layers are not single isolated or post-depositional replacement events, but chemical precipitates that sequentially sedimented out of the water column. Red colour in Panels (B) and (C) depict Fe and green in panels (C) and (F), Si.

1584

1585

Solid Earth
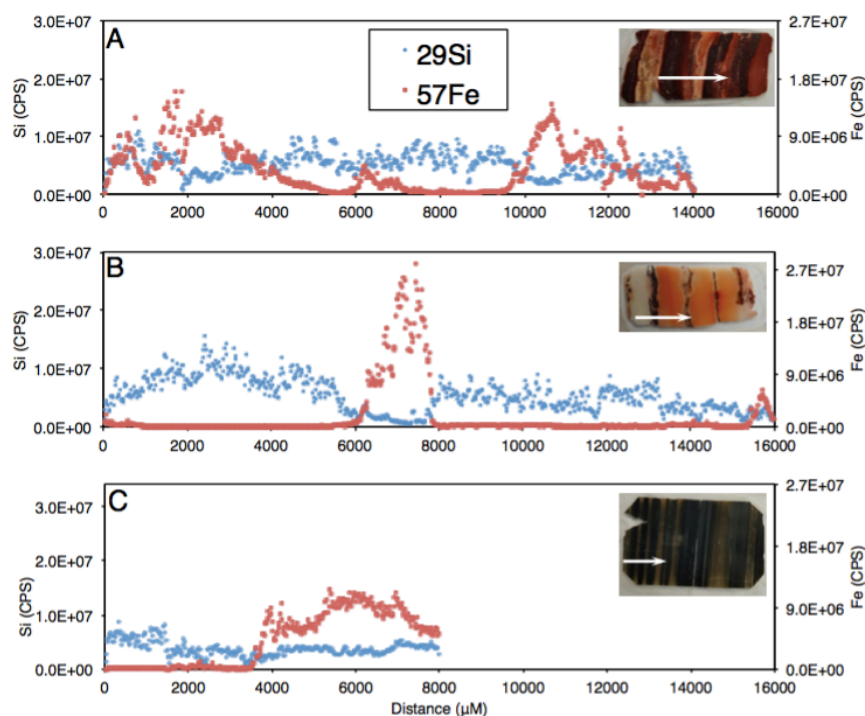Discussions

Open Access

EGU
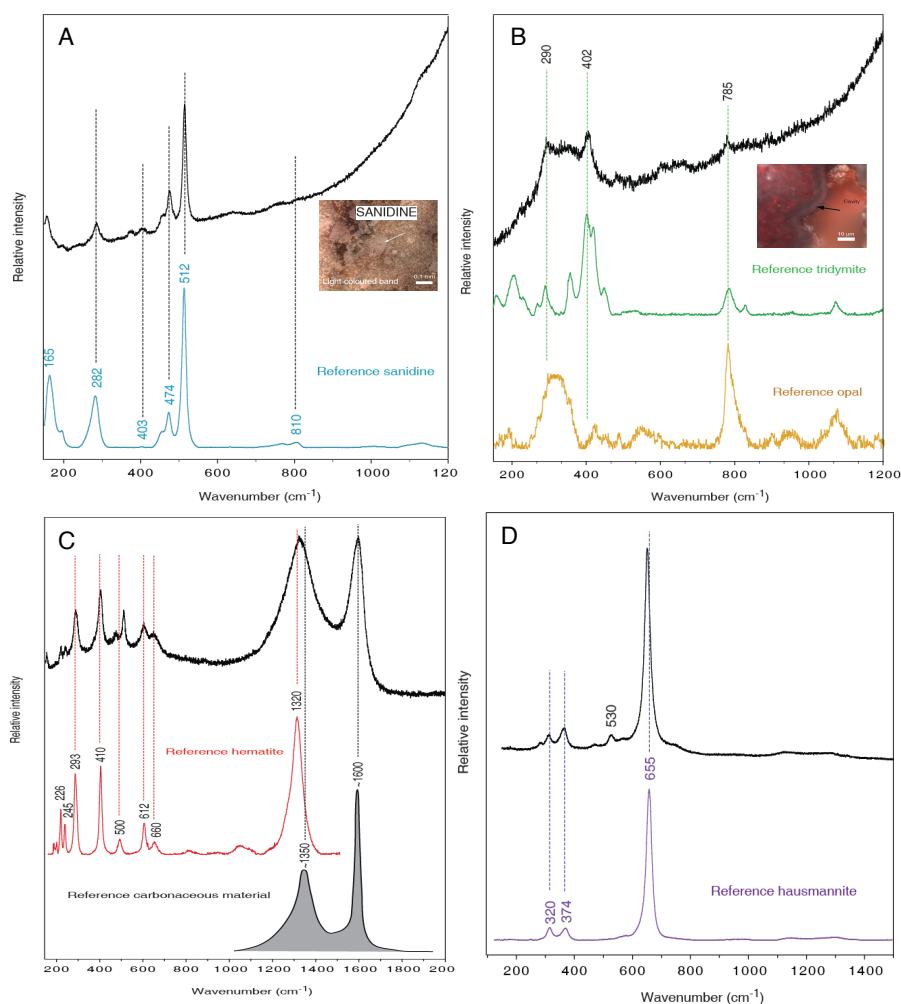
Fig. 10. Raman spectroscopy of the Fe- and/or Si-rich bands from NFIF.

1586

1587

1588

Solid Earth
Discussions
Open Access
EGU

1589

1590 Fig. 11. Fluctuation in Si and Fe content measured by in situ laser ablation ICP-MS
1591 analysis. (A), Milos BIF-type rock with evenly distributed Si and iron rich bands. (B),
1592 Milos BIF type rock with large Si bands (whitish-brownish strips) and narrow Fe-rich
1593 bands (dark strips). (C), An example for the 2.5 Ga Kuruman BIF. Insets are analyzed
1594 thin sections. For scale, each thin section is ≈3.3 cm long. White arrow on thin section
1595 indicates analyzed area.
1596

1597
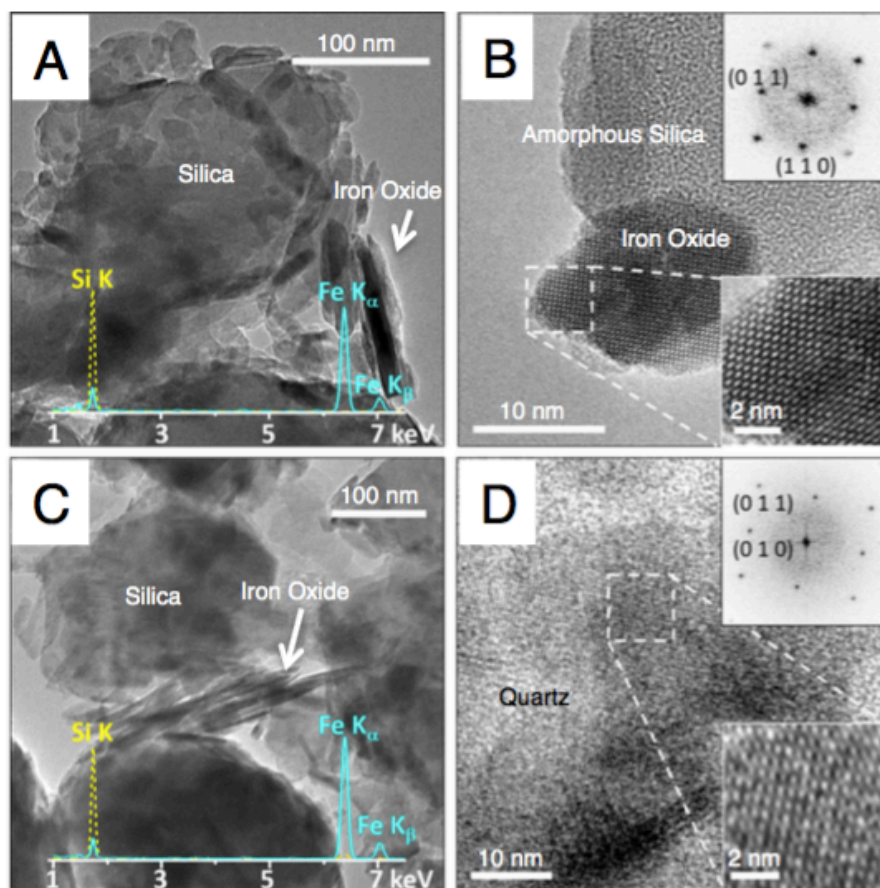
Fig. 12. TEM characterization of an NFIF and MFIF specimen. (A) lower magnification MFIF TEM-BF image. (B) High resolution images of NFIF showing amorphous Si and iron oxide crystallline lattice structures. Insets highlight a hematite particle viewed from the [1-11] axis (Rhombohedral lattice). (C) Lower magnification MFIF TEM-BF image. (D) High resolution images of MFIF showing crystalline quartz and iron oxide crystallline lattice structures. Insets in (D) show a quartz crystal viewed from the [100] axis. Both samples contain silica with a few hundred nm particle size, and smaller needle-like iron oxide particles. Spectral lines in panels (A) and (C) are X-ray Energy Dispersive elemental profiles of the individual Fe and Si mineral phases.
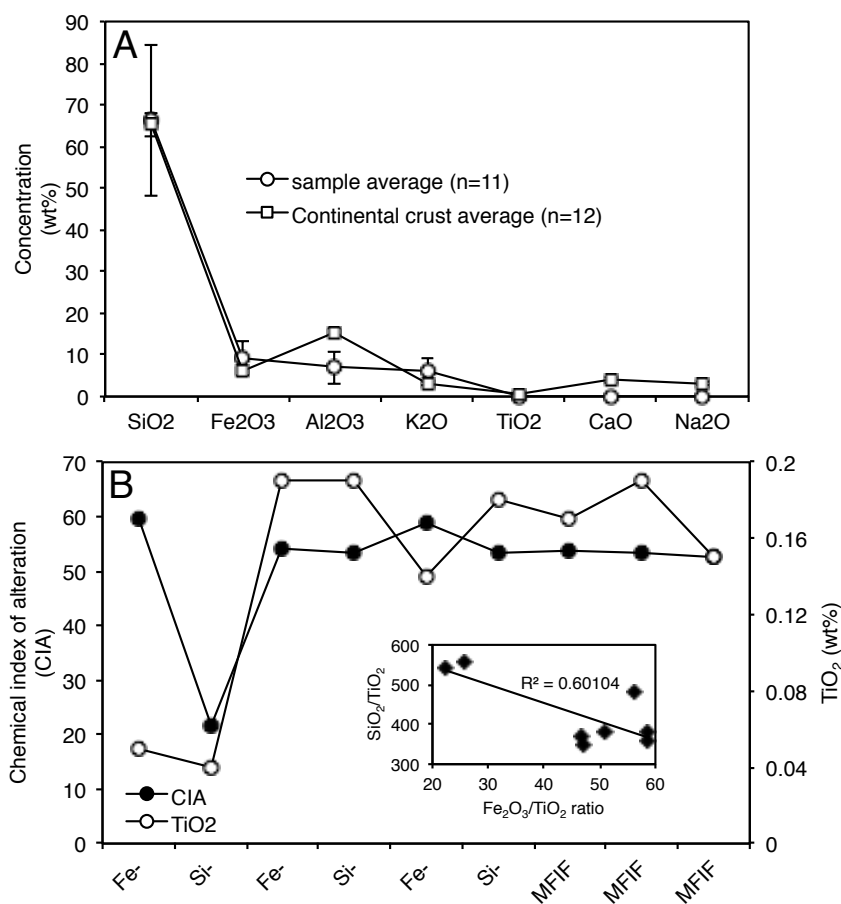
1611

Fig. 13. Bulk average concentrations of major trace elements and chemical
weathering indices. (A), Relationship between average major trace element content
and average continental crust (Rudnick and Gao, 2003). (B), Chemical index of
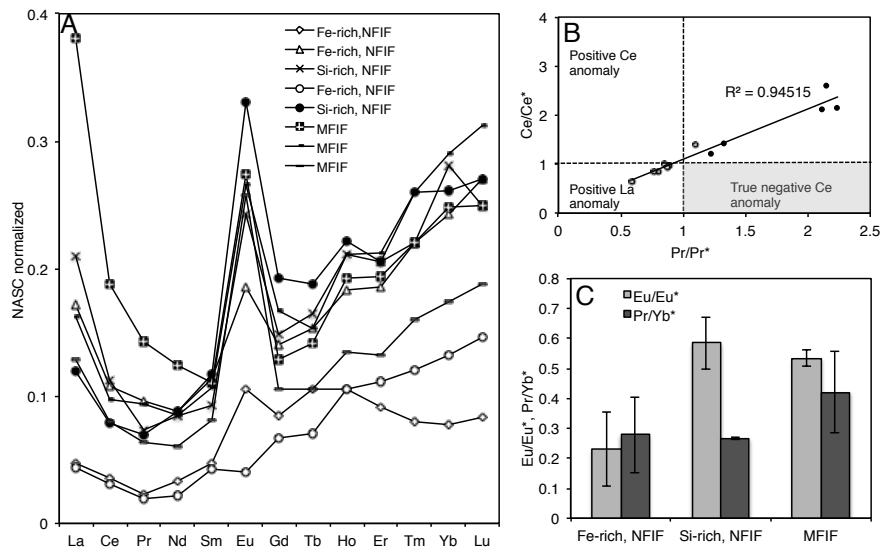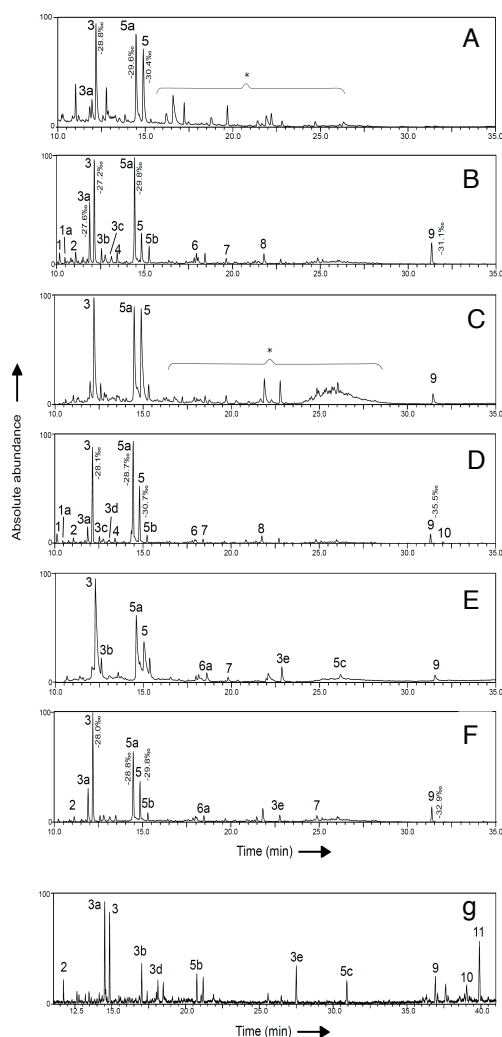alteration (CIA). Inset, relationship between SiO_2 and Fe_2O_3.

1612
1613
1614
1615
1616

1617

Solid Earth
Discussions

1618

1619   Fig. 14. Rare Earth Element (REE) distribution in samples and calculated Ce and Eu
1620   anomalies. (A), NASC normalized REE distribution in various rock facies. (b), Ce
1621   and Eu anomalies. (C), Eu anomalies and light REE (LREE) vs. heavy REE (HREE).
1622

1623

Fig. 15. GC/MS chromatogram sections of total lipid extracts of the BIF (A-F) for
bands excised from the sawn rock in Figure 2c. Panel G illustrates a total lipid extract
of modern sediment from the Milos basin. Values beside peaks indicate the lipid $\delta^{13}C$
values due to the low intensity of the lipids recovered this was not possible for all
peaks. Peaks have been annotated as the following compounds (FAME = fatty acid
methyl ester, Me = methyl group, TMS = trimethylsilyl, TMSE = trimethylsilyl ester):
(1) $C_{14:0}$ FAME, (1a) $C_{14:0}$ 13Me FAME, (2) $C_{15:0}$ FAME, (3) $C_{16:0}$ FAME, (3a) $C_{16:9}$
FAME, (3b) C16:0 TMS, (3c) 10Me $C_{16:0}$ FAME, (3d) $C_{16:9}$ FAME, (3e) $C_{16:0}$ TMSE,
(4) $C_{17:0}$ TMS, (5) $C_{18:0}$ FAME, (5a) $C_{18:9}$ FAME, (5b) $C_{18:0}$ TMS, (5c) $C_{18:0}$ TMSE, (6)

1634 $C_{19:0}$ FAME, (6a) $C_{19:0}$ 18Me TMS, (7) $C_{21:0}$ TMS, (8) $C_{22:0}$ TMS, (9) Cholesterol
1635   TMS, (10) Stigmasterol TMS, (11) beta-Sitosterol (*) Contaminants e.g. phthalates.
1636

1637
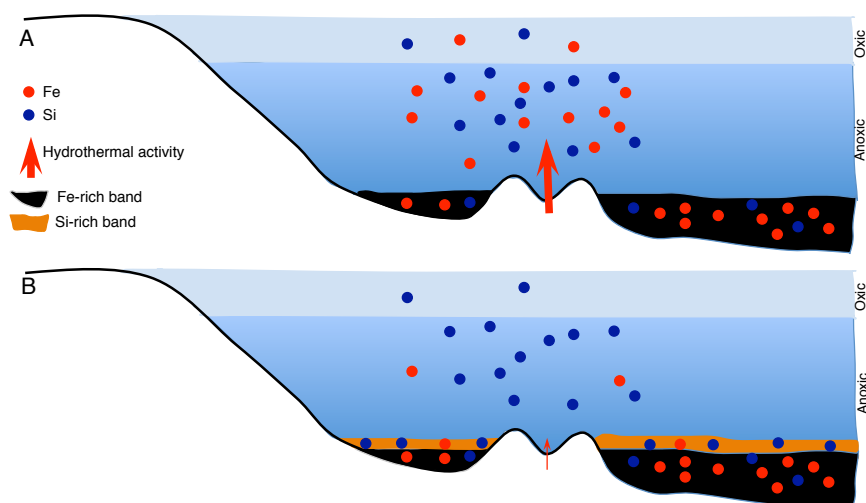
1638

1639   Fig. 16. Conceptual model showing the mechanism of band formation in the NFIF
1640   related to changes in the intensity of hydrothermal activity and chemical oxidation of
1641   Fe(II) to Fe(III) in the water column, inferred directly from our data. See Chi Fru et
1642   al. (2013) for a biological model for the formation of the MFIF.